ISOPOD: **Iso**lating **P**oled **O**n-chip **D**evice

Clayton Cheung[1], Matthew Ai[1], Onkar Apte[1], Juan Garcia Nila[1],

[1]*Ming Hsieh Department of Electrical and Computer Engineering,*
University of Southern California, Los Angeles, California 90089, USA.

December 13th, 2023

Contents

Chapter 1

Introduction

We propose a novel circuit for a non-ferromagnetic, on-chip microwave isolator. Isolators are essential in the amplification chain for qubit readout to block amplifier backaction and protect fragile RF components from unintentional back propagating noise. One challenge with current ferrite isolators/circulators is that they are bulky and use large magnetic components, which can introduce loss. Bulkiness is a problem for scaling up a quantum computer. Furthermore, magnetic flux can get trapped within the superconductor, harming qubit performance. Thus, on-chip isolation can benefit the field of cQED and bring us closer towards the goal of fully on-chip qubit amplification and readout.

1.1 Report structure

This report is structured as follows. In Chapter 2, we discuss the current state of isolators. In chapter 3, we talk about relevant prior works. In chapter 4, we give a one-paragraph overview of our idea; in chapter 5, we build and explain our idea rigorously. In chapter 6, we show the numerical analysis and simulations that we perform. Chapter 7 briefly discusses how we chose our circuit parameters based on current technology. Chapter 8 has our results, figures of merit, and pertinent discussion. Chapter 9 looks ahead to what further work we can do. Appendix A has derivations of our nonlinear wave equation in our structure, and Appendix B contains the coupled mode equations needed for simulation.

1.2 Notation and conventions

In this report, we have used *two* different definitions for the relationships between pump, signal, and idler. In Chapter 3, we use $f_s + f_p = f_i$, which we prefer as a more "intuitive" definition as the pump tends to be an input of the system, and the idler should be an output in everyday language.

However, after Chapter 3, due to conventions used by the works that we most heavily referenced throughout this project, we use $f_s + f_i = f_p$ for our numerical simulations of theoretical equations as well as our time-domain circuit simulations, and not $f_s + f_p = f_i$.

Chapter 2

Current state of isolators

Isolators rely on breaking the time-reversal symmetry inherent to Maxwell's equations of electrodynamics. Various methods utilizing active and passive devices have been proposed in the past few decades. Most notably, ferrite materials are used to impart a direction-dependent phase shift on the incoming electrical signal, which can be engineered to create constructive or destructive interference of the signal. However, due to their general incompatibility with quantum computing applications, various other methods for creating isolation and circulation have come up. Notably, parametric frequency conversion imparts different phases to our signal depending on the direction of energy transfer between frequencies.
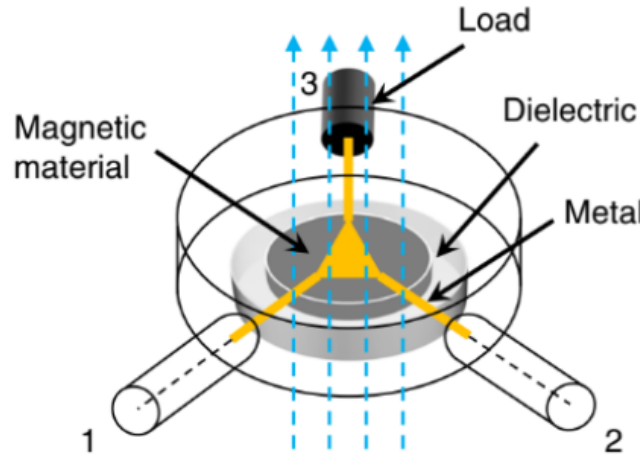

Figure 2.1: Example of bulk ferrite isolators from [1]

Aumentado demonstrates a field-programmable Josephson amplifier [2] that relies on destructively interfering signals from different frequency conversion paths to achieve isolation. Other novel methods include a dynamic modulation switch-based isolator from Chapman [3], a synthetic rotation-based isolator with already circulating modes to break rotational symmetry [4], and optomechanical transduction [5]. A previous approach most similar to ours is from Ranzani et al. [6], which utilizes a co-propagating tone to modulate phase matching to produce unidirectional frequency conversion. All these methods rely on providing isolation either through unidirectional phase matching, time-dependent modulation, or interference with asymmetrical phases. Our proposed device, ISOPOD, does not fall neatly into any of these categories but utilizes a concept similar to quasi-phase-matching, which is described later. However, all these nonreciprocal devices share the use of nonlinearity to break time-reversal symmetry. Asymmetric electric field distributions, either in space or time, provide the means by which phase or nonlinear frequency conversion is direction-dependent.
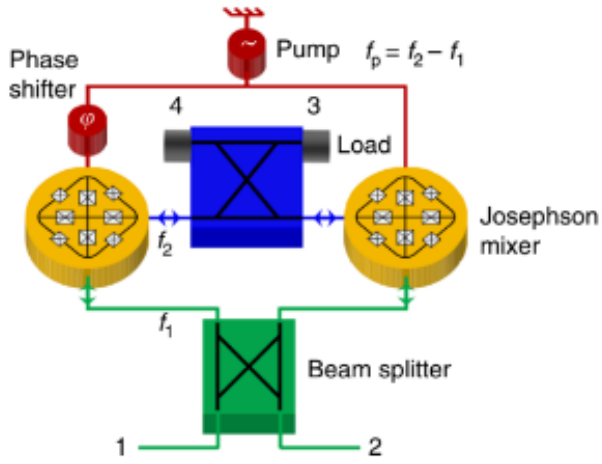
(a) Interferometric Isolator [1]
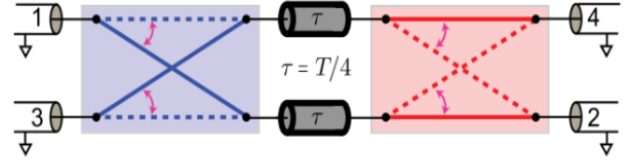
(b) Active Modulation-based Isolator [3]
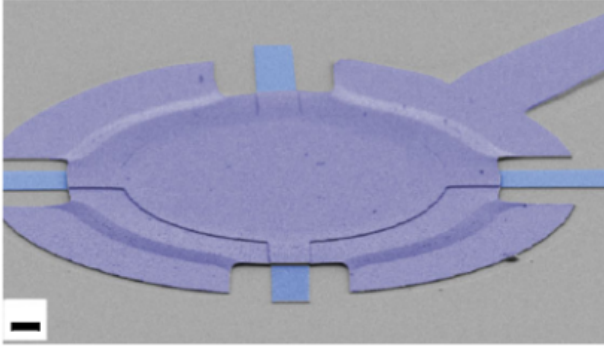
(c) Optomechanical Isolator [5]

(d) Unidirectional Frequency Conversion [6]

Figure 2.2: Present state-of-the-art approaches for On-chip isolators

3

Background

In this chapter, we discuss parametric nonlinear devices proposed in prior works whose theories of operation are highly important to our work.
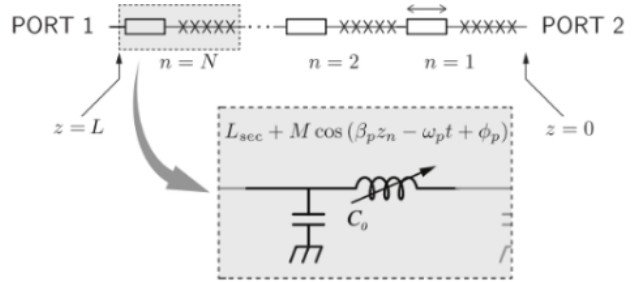
Parametric frequency converters typically operate either in a resonator-based structure or a traveling wave structure. Resonators, if fabricated with high quality factor Q, enhance nonlinear effects like frequency conversion because the electromagnetic field can be confined tightly and have a more effective nonlinear interaction length. However, resonators have inherent bandwidth limitations, simply by geometry—they can only host a narrow range of frequencies within.

To resolve this, we can "unravel" a resonator into a traveling-wave geometry where our interacting signals must co-propagate. This is the principle behind the design of traveling-wave parametric amplifiers (TWPAs). In any travelling-wave-based nonlinear parametric process, **phase-matching** is crucial to maximizing nonlinear conversion in all fields—be it in nonlinear optics or superconducting circuits. Phase matching is necessary in the presence of dispersion, which is when the speed of the propagating signal varies with frequency. Without phase matching, power between our waves will periodically transfer back and forth, leading to no net transfer of power, which can be seen from the coupled-mode differential equations (CMEs) that describe the field amplitudes of the waves.

Various methods of phase matching exist, which all essentially reduce to controlling the speed of the signals to different frequencies to compensate for dispersion, whether that is adjusting the index of refraction in optics or modifying the inductances and capacitances of a transmission line. Another approach is quasi-phase-matching (QPM), which is a well-known technique in optics to perform phase matching **without** engineering the waveguide's geometry, but it has not been heavily explored in superconducting circuits and transmission lines until recently by Zorin [7]. In optics, a common technique for QPM is **periodic poling** of nonlinear ferroelectric materials such as lithium niobate ($LiNbO_3$), which exhibit second-order nonlinearity, or $\chi^{(2)}$ nonlinearity. The resulting system is commonly known as periodically-poled lithium niobate (PPLN). Poling is typically used to enhance nonlinear wave mixing and harmonic generation, but has more applications beyond this.

Poling opens up the opportunity to use poling defects, which have been demonstrated in integrated photonics to be capable of creating interesting devices like ultra-fast low-energy switches [3] and optical diodes [8].

We will explore the optical diode concept from Katia Gallo's 2001 paper [8] as it provides a

novel method for nonreciprocal frequency conversion when extended to the microwave domain. While poling in optics works by inverting ferroelectric domains to reverse nonlinearity, poling in superconducting circuits is significantly different in the fundamental physics. Still, the work by Zorin [7] demonstrates that poling is possible in superconducting circuits, and hence, we aim to combine these two concepts to create an on-chip unidirectional frequency converter, which can hopefully be extended to an isolator/circulator with diplexing or even a directional parametric amplifier in the future.

3.1 Ranzani et al. (2017)

In [6], they propose a directional frequency converter, the same as us, but the working of their device is completely different from our proposal. They achieve frequency conversion by utilizing a "control" transmission line signal such that when the signal co-propagates with the control line pump, the signal converts to the idler as phase matching is achieved. In the reverse direction, the counter-propagating pump will not satisfy the phase-matching condition as the wave vector k_{pump} of the pump will have the sign flip, and thus, there will be no frequency conversion. Essentially, the non-reciprocity arises from the nonreciprocal nature of the modulation from the control line, as the inductance of the line is dependent on the co-propagating pump. The transmission line is populated with arrays of Josephson junctions which act as nonlinear inductors and these circuit elements provide the nonlinearity needed for unidriectional frequency conversion.

3.2 Gallo et al. (1999) and (2001)

The works [9] and [8] propose the use of an optical crystal with asymmetric poling defects. By exploiting this asymmetry, their proposed device enables the efficient conversion of incident light into second-harmonic waves in one direction while inhibiting this process in the opposite direction, thus establishing a diode-like behaviour based on QPM.

The intuitive explanation comes from treating the poled region like "switches" [3]. With a poling defect, the pump and idler swap places, since one region is not quasi-phase-matched while the rest are; so, our nonlinear process goes from upconverting our pump and signal into an idler, to downconverting our idler back into the pump and signal. (Note that this is using the definition where idler is the sum of signal and pump, to be contrasted with a different definition in the rest of our report.) This poling defect leads to a phase shift that changes the direction of power transfer between frequencies. By placing this defect asymmetrically, it is possible to upconvert the majority of our signal in one direction, whereas in the opposite direction, the signal stays at the same frequency. The mathematics behind the required phase shift needed to impart this change in conversion between frequencies is much more involved as Gallo numerically optimizes the phase difference needed to create isolation, but the overall concept is the same.

3.3 Zorin et. al. (2021)

Zorin [7] proposes a Josephson TWPA operating operating in the three-wave mixing mode which can implement quasi-phase-matching. So far, all the techniques mentioned apply to optical systems, but we aim to extend this work to superconducting circuits, which has been shown to be possible in [7]. In their design, the nonlinearity of the transmission line is analogous to a $\chi^{(2)}$ crystal, and flipping the RF SQUID configuration periodically in the presence of a static
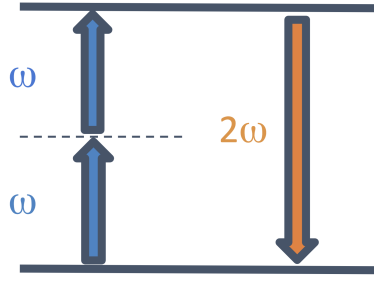
Figure 3.1: Frequency conversion in 3WM Second Harmonic Generation, where $f_s + f_p = f_i$

magnetic flux bias can mimic the periodic poling of $\chi^{(2)}$.

Mathematically, this flip in the nonlinear coefficient will yield the same result as in the optical case and quasi-phase-matching can be achieved. However, the physics explaining this phenomenon is completely different, as nonlinearity in optics arises from an anharmonic oscillator model of polarization in Maxwell's equations, and nonlinearity in superconducting circuits arises from the current-phase relationship of Josephson junctions. Regardless of the origin, we can treat these two devices similarly, as they follow the same differential equations for the field amplitudes. **Knowing this, we investigate the idea that it is possible to engineer various periodically poled optical devices in the superconducting regime, such as the optical diode proposed byGallo in 2001 [8].**

Figure 3.2 is an image of their proposed following circuit, which acts like a periodically poled $\chi^{(2)}$ crystal:
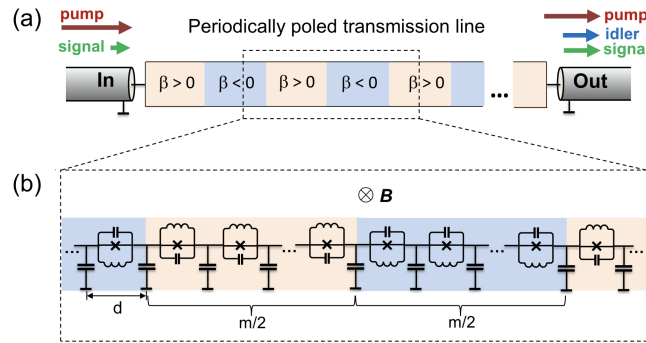
Figure 3.2: Periodically poled waveguide circuit by [7]

3.4   Dixon. et. al. (2020)

T. Dixon [10] does a deep analysis of three-wave mixing in JTWPAs by comparing circuit simulations using *WRspice* and coupled mode equations (CMEs). They find that the CMEs that account for fifth-level harmonics most accurately model the *WRspice* results. Since circuit simulations allow for the propagation of all the tones, he concludes that he needs to allow up to five tones in the CMEs to match both methods when considering a large TWPA length. In a textbook analysis of coupled mode equations for nonlinear wave mixing, typically only the pump, signal, and idler are required, but many higher order tones are needed for a full numerical analysis, according to Dixon, to fully capture the JTWPA behaviour.

Dixon's approach is the basis for our simulations of device performance. To optimize the transmission from the forward direction in comparison with the backward direction, we first solve numerically the fifth-order coupled mode equations (CME-5) to find the input parameters on *WRspice* simulations. We follow the same steps as Dixon to also numerically simulate our device with *WRspice*.

CME-5 incorporates the modes related to the frequencies $\{\omega_i, \omega_s, \omega_s, \omega_p + \omega_i, \omega_p + \omega_s, 2\omega_p, 2\omega_p + \omega_i, 2\omega_p + \omega_s, 3\omega_p, 3\omega_p + \omega i, 3\omega_p + \omega s, 4\omega_p, 4\omega_p + \omega_i, 4\omega_p + \omega_s, 5\omega_p\}$. We have included the explicit equations in Appendix B.

Chapter 4

Overview of our idea

We propose a non-reciprocal, directional frequency converter that leverages a poling defect, relying on quasi-phase-matching principles. Then, we exploit this non-reciprocity to create an isolator.

Our idea is to implement a directional frequency converter by creating an asymmetric device based on the idea from Gallo et al. (1999) [9] and (2001) [8], using techniques described by Zorin et al. (2021) [7] to generate asymmetry. By inverting the flux biasing of a section of SQUIDs in the Josephson transmission line proposed by Zorin [7], we mimic "poling" from nonlinear optics and expect to create a similar isolation effect. In order to accurately simulate this device, we follow a similar approach to [10], which utilizes the circuit simulator *WRspice*. In addition to *WRspice*, Dixon [10] notes that he needs to consider up to five tones (higher harmonics) in the coupled mode equations to match the continuous solution with the discrete lumped element circuit simulation, so we do the same.
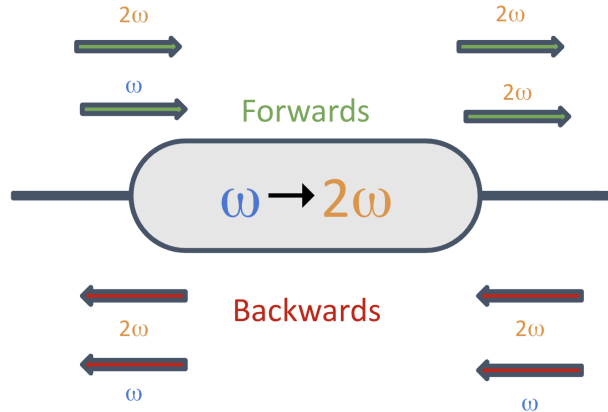
Figure 4.1: Unidirectional frequency converter implementing second harmonic generation

Chapter 5

Device Proposal and Numerics

Assume that we have a perfectly periodically poled waveguide as follows:
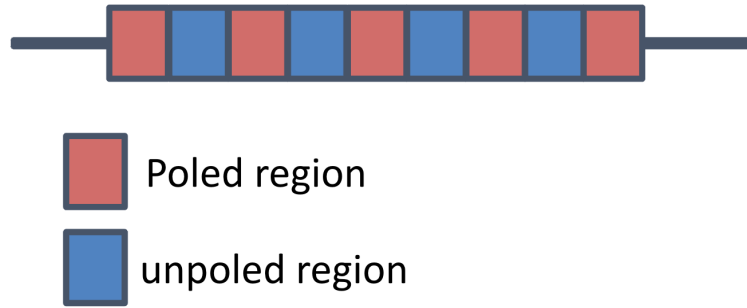
Figure 5.1: Poled waveguide

Now, let

$$\omega_s = \text{Signal frequency} \,, \tag{5.1}$$
$$\omega_p = \text{Pump frequency} \,, \tag{5.2}$$
$$\omega_i = \omega_p - \omega_s = \text{Idler frequency} \,. \tag{5.3}$$

From here onwards, left-to-right is the forward direction, illustrated in green, and right-to-left is the backward direction, illustrated in red.

Now, in the case of a periodically poled waveguide, there is no reciprocity, and this waveguide acts as a bidirectional frequency converter.

Figure 5.2: Input-outputs in both directions for a poled waveguide

Now, assume that we have poling as follows:

Figure 5.3: Waveguide with a poled section at the beginning

In this case, we can get directional frequency conversion as explained in Gallo's papers [9] and [8] and shown ahead in Fig. 5.4. As mentioned before, the spatial asymmetry of the nonlinear medium means that forward propagating light will interact with the poled region first while backwards propagating light interacts with the poled region last. In this way, our nonlinear 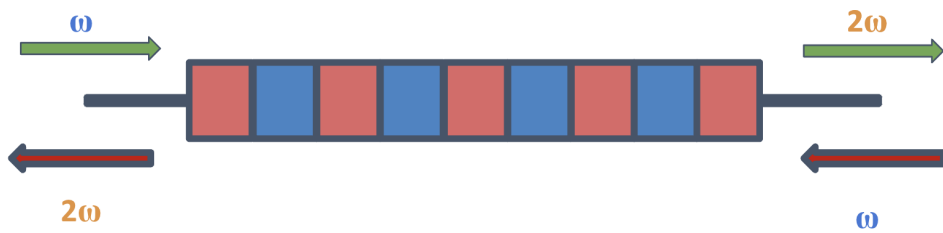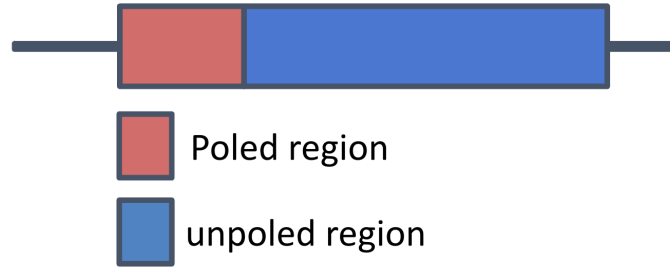interactions are asymmetric as our system is spatially asymmetric. From an engineering perspective, we chose second harmonic generation (SHG) to be the nonlinear process as we cannot be certain of the reflected noise frequency. In this way, the reflected noise can act as its own pump. Otherwise, an external pump tone would need to co-propagate with the noise to attain nonlinear conversion, which would not be ideal.
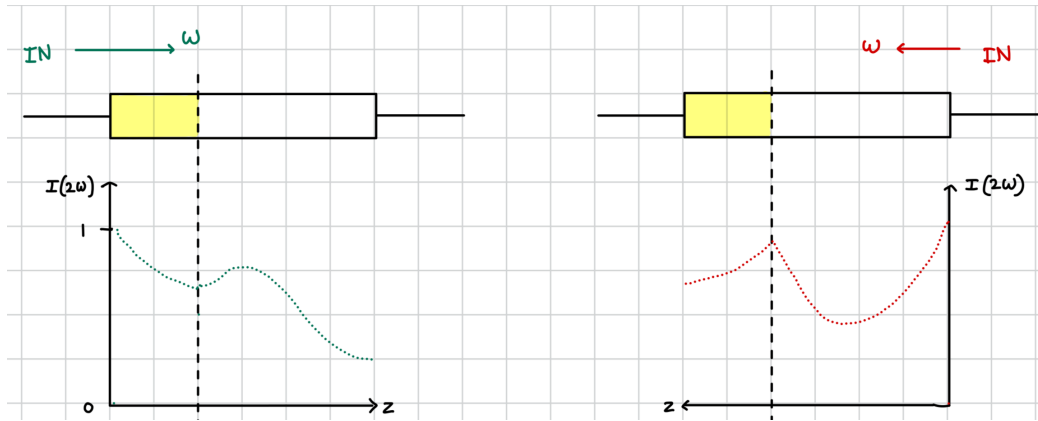
Figure 5.4: Intensity plots for 2ω in both directions

Therefore, ideally, the signals in both forward and backward directions will behave as follows in the following Fig. 5.5:
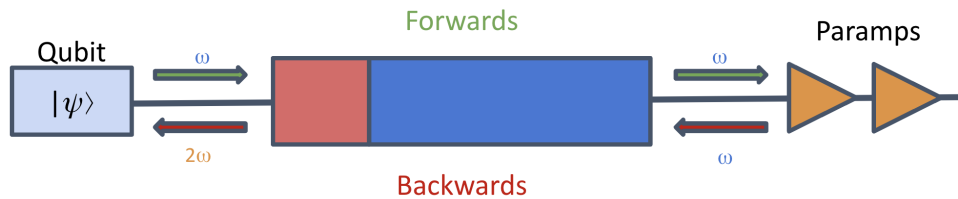
Figure 5.5: Input-outputs in both directions waveguide with a poled region, which gives us non-reciprocity, unlike Fig. 5.2

Now, let's see with an intuitive example, how/why exactly do we get non-reciprocity due to this special asymmetry shown in Fig. 5.5.

11

(a) reciprocal
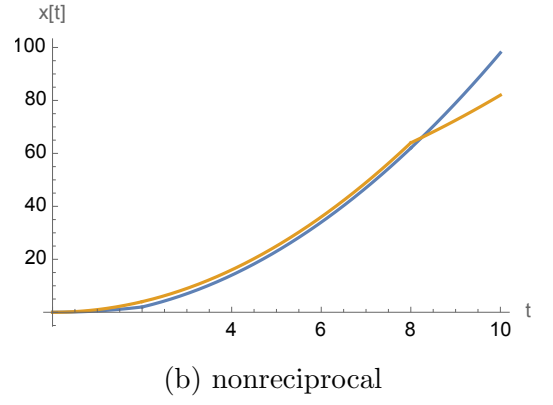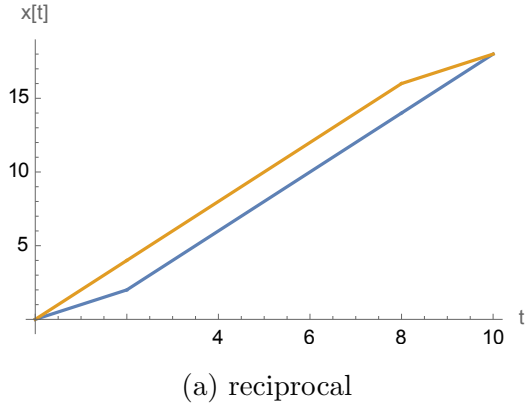
(b) nonreciprocal

We can do an analogy between the non-reciprocity and the linear motion. Let us assume there are two characters: Alice and Bob; while Alice goes from A to point B, Bob travels it backwards from B to A. We want to see who makes it first to its end. In the first case, Alice goes slowly at a constant velocity during the first t_1 minutes, and then he runs at a higher constant pace to reach its end, while Bob decides to run first at a higher pace in the first $T - t_1$ minutes and take the last t_1 minutes at a slower rate as seen in Fig. 5.6a. As you can note, both of them reach their destination at the same time.

On the second case, let's repeat the first case, but now they become accelerated. Still, Alice accelerates at a slower rate during the first t_1 minutes and then accelerates at a higher rate afterwards. A similar case will happen to Bob, but with $T - t_1$ as the transition time, as you can see from Fig. 5.6b, we know they do not reach their destiny at the same time. This analogy can help you understand the intuition behind our device.

Chapter 6

WRspice Simulations

We used *WRspice* to simulate our circuit designs. *WRspice* is a software package based on Berkeley SPICE3, with added support for the simulation of non-linear circuit components, including Josephson junctions.

Let's define a circuit "cell". These are basically the same modular elements of a flux-biased JTWPA [11]. We use two types of cells in our circuit; let's call them "+" cell and "−" cell. The only difference between these two cells is the direction of the flux biasing.
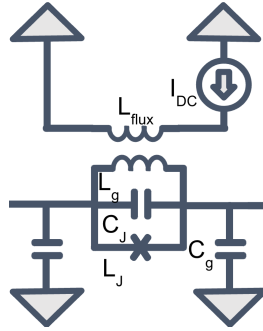

Figure 6.1: Circuit cell

We combine a number of "+" cells and "−" cells to create our device. The explicit circuit design that we use to run our simulations is as follows:
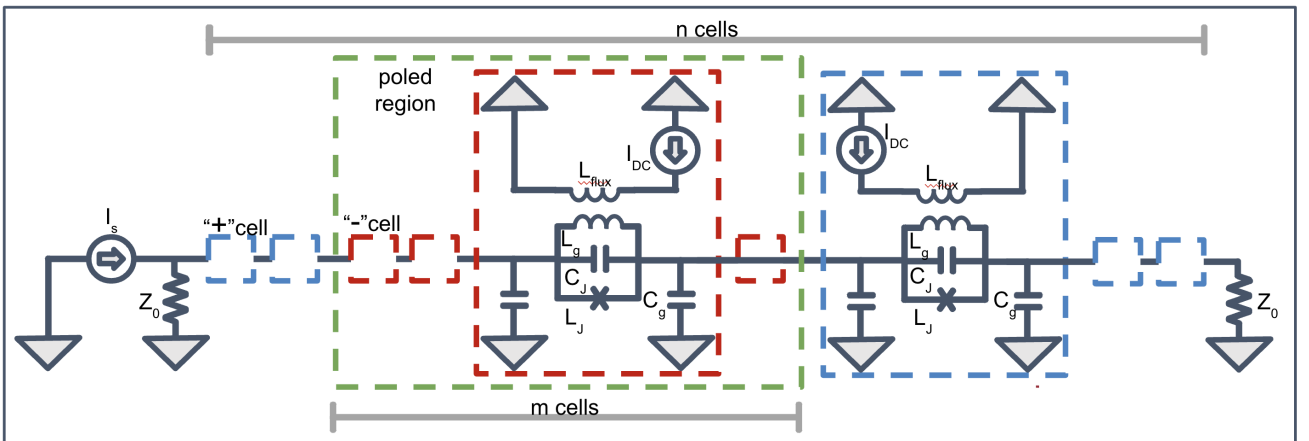

Figure 6.2: Complete circuit schematics for ISOPOD

Here, I_p and I_s are pump and signal current sources, respectively. Z_0 are the termination resistances, with values chosen to match the device's wave impedance. The cells marked in red are the "−" cells, and the cells marked in blue are the "+"cells. To model the reversed flux biasing for "−" cells, we simply invert the DC current source I_{dc} compared to the "+" cells. In general, our "poled" device has a total of n cells, and has inverted flux biasing for m cells, between some nodes a and $b = a + m$. These m cells make the "poled" region.

Now we briefly describe the symbols/variables for our parameters and components. We discuss the outcomes of both the following simulations in chapter 8.

n = total number of nodes

m = number of nodes in the poled region

L_g = geometric inductance

C_g = capacitance to the ground

C_J = capacitance of the JJ in the model

L_J = Josephson inductance

I_p = pump current (current source)

R_term = resistance of the termination resistor

a = starting cell number of the poled region

b = ending cell number of the poled region

I_s = signal current (current source)

I_{dc} = DC current bias

I_crit = Josephson junction critical current

f_p = frequency of the pump

f_s = frequency of the signal

6.1 ISOPOD simulation 1

For our device presented here, we use the following parameters for the simulation of the circuit given in Fig 6.2:

$$n = 1250 \tag{6.1}$$
$$a = 1 \tag{6.2}$$
$$b = 208 \tag{6.3}$$
$$m = 208 \tag{6.4}$$
$$R_\text{term} = 23.8747\ \Omega \tag{6.5}$$
$$L_g = 57\ \text{pH} \tag{6.6}$$
$$C_g = 100\ \text{fF} \tag{6.7}$$
$$C_J = 60\ \text{fF} \tag{6.8}$$

$$L_J = 57\ \text{pH} \tag{6.9}$$
$$I_p = 0\ \text{A} \tag{6.10}$$
$$I_s = 0.6 \times 10^{-6}\ \text{A} \tag{6.11}$$
$$I_{dc} = 14.0680 \times 10^{-6}\ \text{A} \tag{6.12}$$
$$I_\text{crit} = 5.0000 \times 10^{-6}\ \text{A} \tag{6.13}$$
$$f_p = 7\ \text{GHz} \tag{6.14}$$
$$f_s = 14\ \text{GHz} \tag{6.15}$$

For each iteration of our device, we perform two *WRspice* simulation runs: to characterize the behaviour of a signal propagating (1) in the forward direction, and (2) in the reverse direction. For the forward direction, the circuit is the same as Fig 6.2; for the backward direction, we detach the current sources I_s, I_p and hook them up to the opposite end of our device.

6.2 ISOPOD simulation 2

$$n = 1250 \tag{6.16}$$
$$a = 1 \tag{6.17}$$

$$b = 500 \tag{6.18}$$
$$m = 500 \tag{6.19}$$

$R_\text{term}, L_g, C_g, C_J, L_J, I_p, I_s, I_{dc}, I_\text{crit}, f_p, f_s$ are all the same as in Simulation 1 from Sec. 6.1. The length of our device is still 1250μm as we set each node to be 1μm.

Chapter 7

Fabrication/ Material stack/ Geometry

Like with any device proposal, we should consider the geometry and material stack in order to make it. In its simplest form, our isolator is a modified Josephson traveling-wave parametric amplifier (JTWPA). Because of this, all fabrication, design constraints, and circuit element values are based on current JTWPA designs that have already been fabricated.

We take Macklin's JTWPA [12] as our standard for the capacitances and inductances that can be fabricated. Similar to Macklin, we can imagine such a device to be fabricated with niobium on silicon. On other platforms, such as aluminium, intrinsic device parameters, such as junction resistance and critical currents, will be affected, so the circuit parameters must all be re-optimized.

Specifically, we simulate a qubit operating at a signal frequency of 7 GHz with a second harmonic frequency of 14 GHz. Our geometric inductance is 57 pH, shunt ground capacitance is 100 fF, junction capacitance is 60 fF, and junction critical current is 5 μA. These parameters allow for a SQUID screening parameter of $\beta_L = 0.866$ and a non-zero phase mismatch, to allow for oscillations in power transfer between frequency modes. The device has 1250 cells which is 1.25 mm. We find that to be reasonable compared to Macklin's JTWPA length of 5 mm.
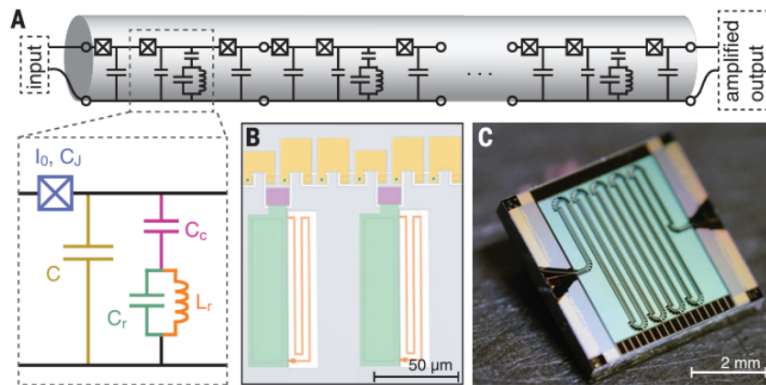

Figure 7.1: Schematic of a JTWPA from which we obtain our circuit parameters [12]

Chapter 8

Results and Figures of Merit

In this chapter, we will talk about the results obtained from simulations described in Sec. 6.1 and Sec. 6.2.

8.1 Results of Simulation 1 (Cells 1 to 208 Poled)

The following tables contain some figures of merit for simulation 1 from Sec. 6.1.

	Forward	Backward
I_{Left}^{ω}	592.56nA	245.71nA
$I_{\text{Left}}^{2\omega}$	3.11nA	134.5nA
$I_{\text{Right}}^{\omega}$	143.32nA	596.27nA
$I_{\text{Right}}^{2\omega}$	230.96nA	2.53nA

Table 8.1: Values of measured current of the left and right endpoints from *WRspice*; forward signal starts at "Left" and backward signal starts at "Right".

	$|S_{21}|^2$ (dB)	$|S_{12}|^2$(dB)
$\omega \to \omega$	-12.33	-7.70
$\omega \to 2\omega$	-8.18	-12.93
$2\omega \to \omega$	33.27	39.74
$2\omega \to 2\omega$	37.42	34.51

Table 8.2: Power ratios. Of special note are the parameters in the second row, which show the amount of 2ω signal generated relative to the inputted ω signal.

From *WRspice*, we can extrapolate forward and backwards insertion losses to quantify our isolation. We use logarithmic power ratios to quantify our results, found simply by squaring the ratios of our measured currents and converting that to dB. Ideally, we would be able to construct a full S parameter matrix to observe the effects of reflections as well as phase relationships, but non-reciprocity can still be demonstrated with power ratios, and limitations with our *WRspice* simulations make phase and reflection data difficult to collect.

The main feature to observe is that our S_{12} and S_{21} parameters are not identical. Mainly, $|S_{12}^{\omega \to 2\omega}|^2$ is -12.93 dB while $|S_{21}^{\omega \to 2\omega}|^2$ is -8.18 dB. **This means we have 4.75dB of isolation**, and while this is not much, it is still a sign of non-reciprocity. Furthermore, our insertion loss in the ω-preserving direction is $|S_{12}^{\omega \to \omega}|^2 = -7.7\,\text{dB}$. Unfortunately, 7.7 dB of insertion loss is not
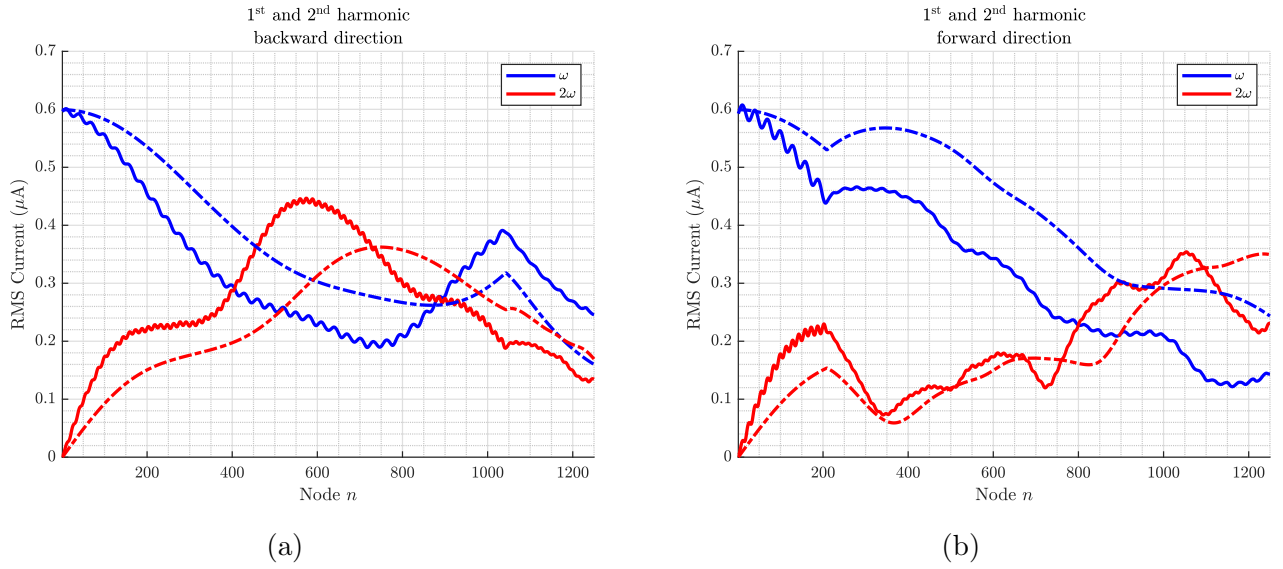
Figure 8.1: Plot of our isolator in the (a) reverse direction and (b) forward direction. Dotted lines are the from CME-5 evaluations from Appendix B, and solid lines are data from *WRspice* simulations from 6.1.

great at all, and we want to get closer to around 1-2 dB insertion loss. We attempted another device simulation, described in the following section, that improved insertion loss, but at the cost of isolation. A full sweep of several parameters will be necessary to truly optimize this value.
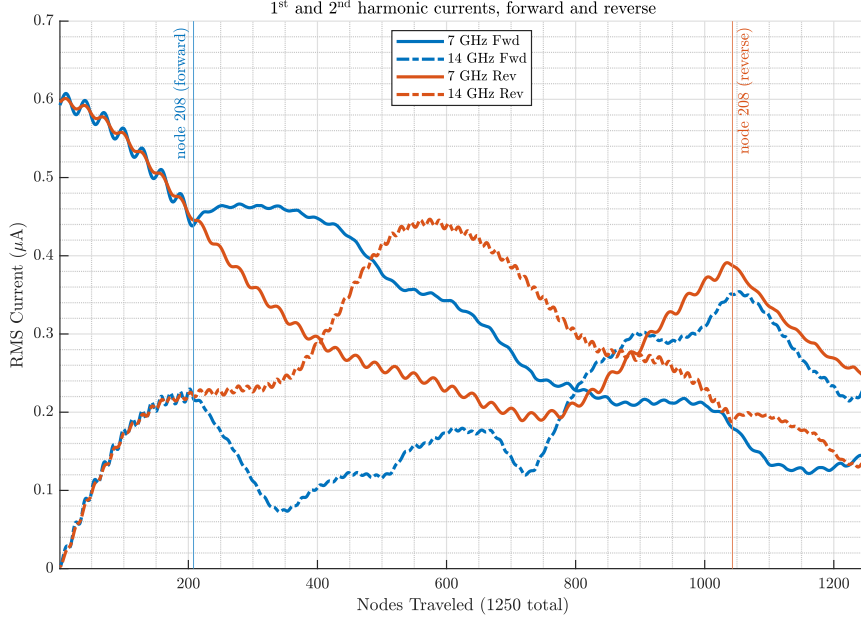
Figure 8.2: Plot combining simulation results in both directions from Sec. 6.1

8.2   Results of Simulation 2 (Cells 1 to 500 Poled)

Now, let's look at the results for simulation 2 given in Sec. 6.2. First, we will see the results from the CME-5 evaluation from Appendix B.

17
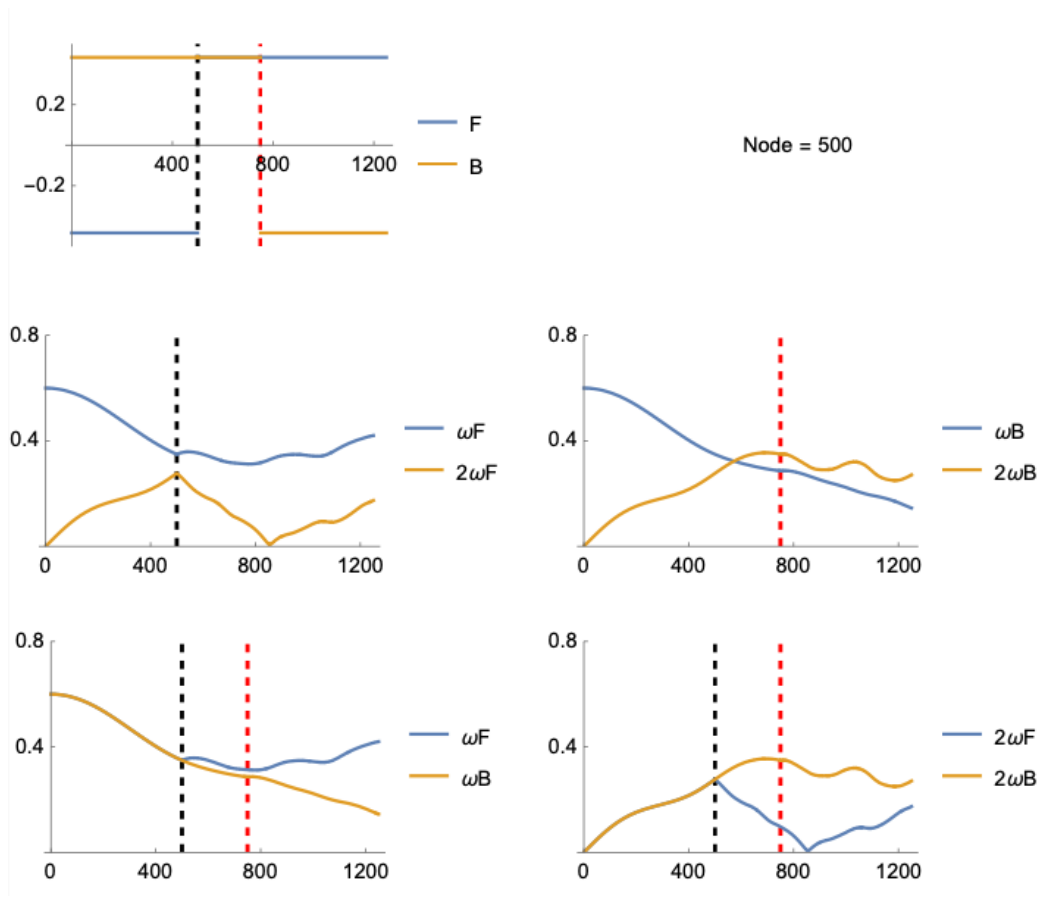
Figure 8.3: Plots showing CME-5 results for Sec. 6.2 in both forward and backward directions for ω and 2ω frequencies, dashed black & red lines are the end of the poled region in the forward and backward directions respectively. F & B in legends are for the forward and backward directions of current propagation.

Now, let's take a look at the results from *WRspice* simulation.
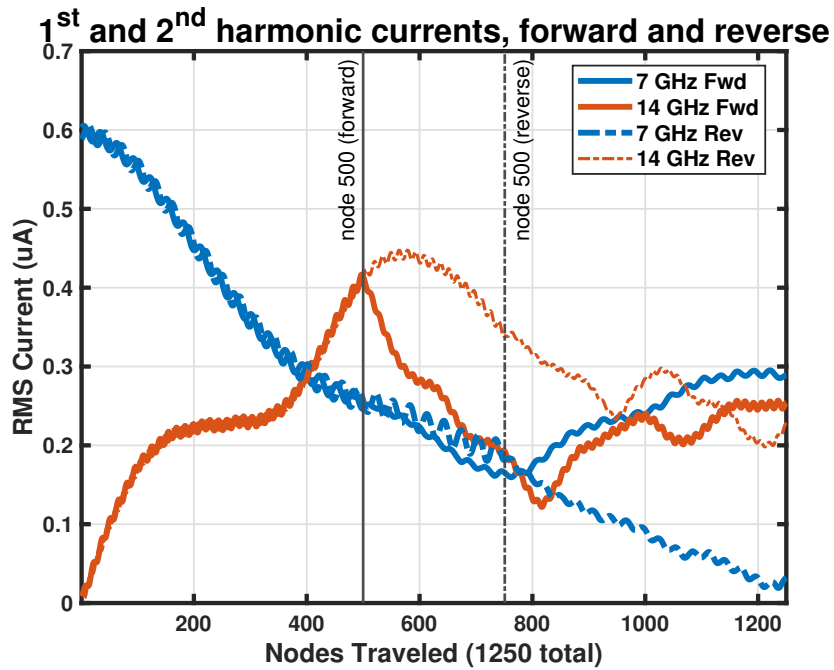
Figure 8.4: Plots showing *WRspice* results for Sec. 6.2 in both forward and backward directions for ω and 2ω frequencies

The following tables contain some figures of merit for simulation 2 from Sec. 6.2.

	Forward	Backward
I_{Left}^{ω} (μA)	0.6034	0.0322
$I_{\text{Left}}^{2\omega}$ (μA)	0.0086	0.2285
$I_{\text{Right}}^{\omega}$ (μA)	0.2889	0.5884
$I_{\text{Right}}^{2\omega}$ (μA)	0.2543	0.0072

Table 8.3: Values of measured current of the left and right endpoints from *WRspice*; forward signal starts at "Left" and backward signal starts at "Right"

	$|S_{21}|^2$ (dB)	$|S_{12}|^2$ (dB)
$\omega \rightarrow \omega$	-6.40	-25.240
$\omega \rightarrow 2\omega$	-7.51	-8.21
$2\omega \rightarrow \omega$	30.51	13.00
$2\omega \rightarrow 2\omega$	29.40	30.03

Table 8.4: Power ratios. Of special note are the parameters in the second row, which show the amount of 2ω signal generated relative to the inputted ω signal.

From *WRspice*, we can extrapolate forward and backwards insertion losses to quantify our isolation.

Here, $|S_{12}^{\omega \rightarrow 2\omega}|^2$ is -8.21 dB while $|S_{21}^{\omega \rightarrow 2\omega}|^2$ is -7.51 dB. **Unfortunately, this means that this device has less isolation than the first one, as this one has only 0.7 dB of isolation.** In contrast to the fist device, our insertion loss in the ω-preserving direction is $|S_{12}^{\omega \rightarrow \omega}|^2 = -6.4\,\text{dB}$; 6.4 dB of insertion loss is a slight improvement compared to 7.7 dB. **On this device, we found the 3dB bandwidth to be roughly 200MHz** by sweeping the signal and pump frequency while fixing the poling region parameters; however, note that we only did this in the coupled-mode equation solver and not WRspice, mainly because we did not have the time to create automated WRspice sweeping code.

These findings tell us that our device in Simulation 1 is actually better for performing frequency conversion. However, ideally we would want to get the insertion loss into the 1 to 2 dB range, to make this device more practically useful.

Further efforts on this device design would entail optimizing this isolation through sweeping the defect width, SQUID screening parameter β magnitude (from eq. A.6), and defect location along the length of the device. The insertion loss is also high, which must be optimized as well. It is likely that higher harmonic tones from the signal and pump are parasitically drawing power away from the fundamental and second harmonic tones, which is also a major contributor to our insertion loss.

9

Future Directions

9.1 Phase Matching

While quasi-phase-matching no longer requires dispersion engineering to phase match, it is important to be able to control the physical size of the coherence length and thus, controlling the phase mismatch Δk is necessary. This boils down to controlling the speed of each frequency and thus is another form of dispersion engineering. It should be noted that if Δk is small, $L_{\text{coherence}}$ will be large, and therefore, we can tune our phase mismatch to adjust coherence length to fit fabrication constraints. In general, if our coherence length is too large, then the device length will become impractical due to how long it will need to be.

9.2 Impedance Matching

Just like in any transmission line, we must be impedance matched to avoid unwanted reflections, which would reduce the isolation ability of our device. For the sake of simplicity, we assume the transmission line before and after our isolator is designed to be 50Ω to be standardized with RF equipment. However, for our optimized isolator parameters, each cell of our transmission line is 23.87Ω.

To resolve reflections, we can adiabatically taper the impedance before and after the isolator in a similar way as [13]. This leverages the small reflection approximation and allows us to transfer our transmission line to a smaller impedance from a larger one with minimal reflections. Ideally, we could engineer the isolator to match the rest of the line at 50Ω, and it will be an important task to consider as one of the next steps.

9.3 Explicit design to make an isolator using our proposed non-reciprocal device

We employ our proposed directional frequency converter to implement an isolator. Currently, we have two ideas in mind, one using a frequency filter and the other using a diplexer (wavelength-dependent multiplexer).

Here is how we use our frequency converter in combination with a filter to achieve isolation in the backward direction:
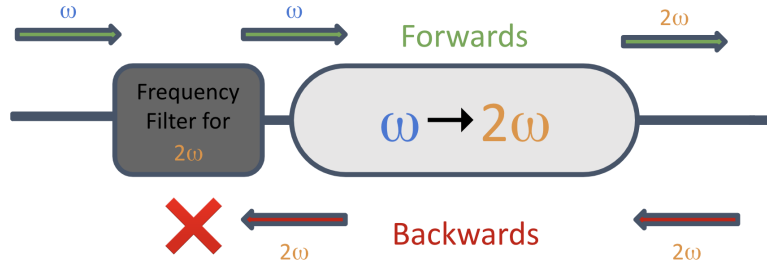
Figure 9.1: Isolator using a frequency filter

Instead of pairing our device with a frequency filter, we can pair it with a diplexer to achieve backward isolation:
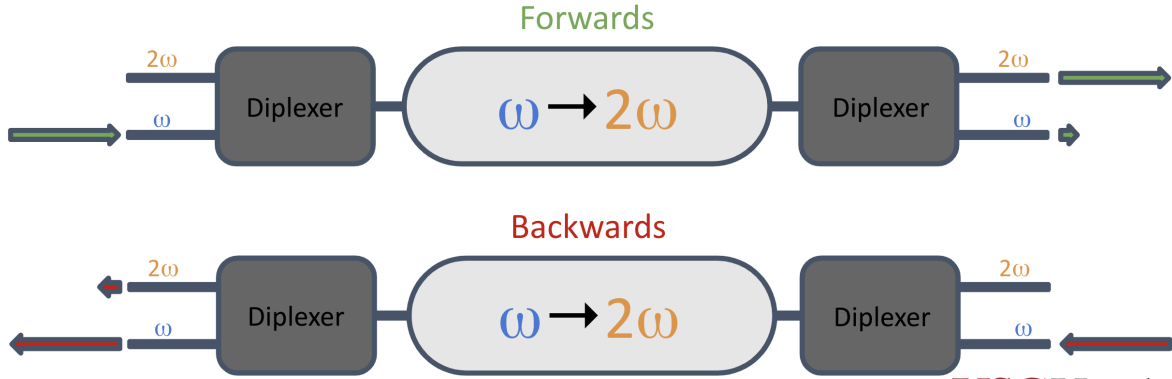
Figure 9.2: Isolator using a diplexer

A diplexer can act as a frequency filter by separating out signals at different frequencies. By cascading diplexers with our unidirectional frequency converter, we can terminate unwanted upconverted tones at 2ω while letting the signal at ω pass through.

9.4 Solving the bandwidth issue

This device suffers from a very narrow bandwidth as the isolation is extremely sensitive to initial conditions such as frequency. In order to solve this, we can envision a series of isolators and diplexers to act as frequency division multiplexing. To scale this device fully, it is likely that many of these isolators will need to be in parallel and connected to a series of diplexers in order to expand the bandwidth capabilities of our isolation.
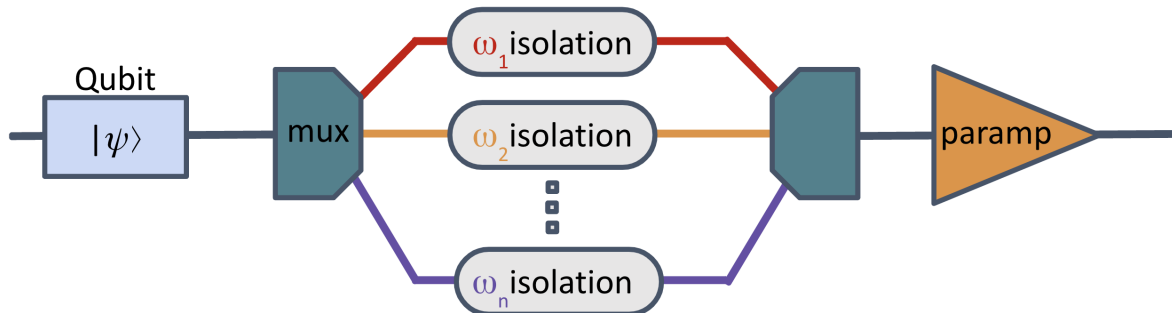
Figure 9.3: Circuit for circumventing the problem of narrow bandwidth

9.5   Combining ISOPOD with an amplifier

Given that our device is nonlinear and is capable of parametric gain, it is not difficult to envision combining this isolator with a paramp to create a fully on-chip directional amplifier. Zorin's device [7] already acts as a TWPA capable of amplification and addition, so further investigation into integrating this isolator at the end of the TWPA can be of interest.

Since the structure is nearly identical in terms of design and fabrication, this isolator could be considered an extension of a larger directional parametric amplifier. It should be noted that this isolator must be used in the non-phase matched regime, so this isolator would work best on a quasi-phase-matched JTWPA like Zorin's.
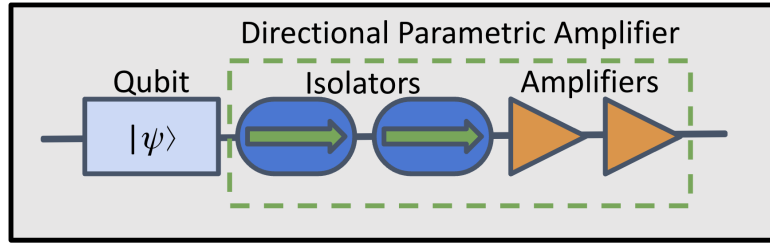
Figure 9.4: Circuit for directional paramp

A

Wave equation from first principles

In this chapter, we discuss the derivation of the non-linear wave equation describing the dynamics of the phase difference from first principles using ideas from the following references [14, 11, 15, 16, 17].

Zorin [11] proposed a ladder transmission line which exhibits both quadratic and cubic Kerr non-linearities using an array of rf-SQUIDS, basically single-junction interferometer [18], connected in series with a central conductor of a coplanar waveguide, which describes a TWPA (travelling wave parametric amplifier) [17].

A.1   RF-SQUID
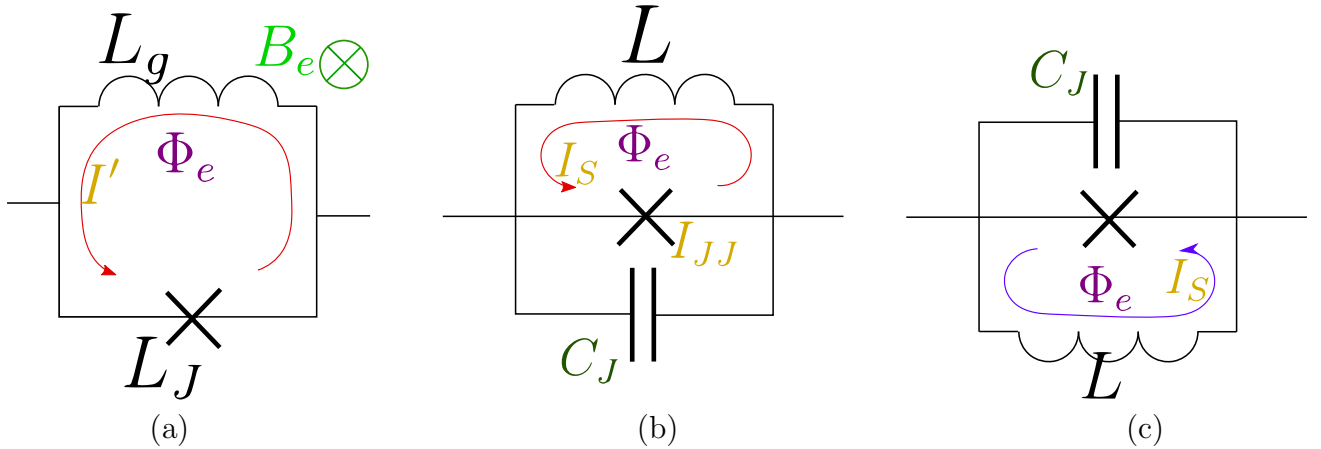
Figure A.1: RF-Squids where Josephson Junctions are the crosses. (a) We see that the contributing terms for the current are due to the external magnetic flux and the JJ (ac) alternating current. Panels (b) and (c) show inverted configurations of rf-SQUIDs, which have opposite signs of quadratic coefficient β. In both cases, the circulating current I_s is anticlockwise [11].

First, we begin analyzing the circuit in Fig. A.1 with Josephson Junction basic equations [18, 19] for the single junction superconducting quantum interference device, or also known as RF-SQUID, by writing the net flux Φ as a function of the external flux $\Phi_e = \int B_e dA$ and the loop current I_l

$$\Phi = \Phi_e - L_g I_l \tag{A.1}$$

where L_g is the geometric inductance of the loop. We can write this equation in terms of the

phase by using

$$\phi \equiv 2\pi \frac{\Phi}{\Phi_0}, \tag{A.2}$$

where $\Phi_0 \equiv \frac{h}{2e} \approx 2.07 \times 10^{-15}$ Wb, is the magnetic flux quantum, so (A.1) becomes

$$\phi = 2\pi \frac{\Phi_e}{\Phi_0} - \frac{2\pi L_g}{\Phi_0} I_l \tag{A.3}$$

hence we note a linear dependence of the phase with the current, and in order to get following exponents, we will use the Josephson junction JJ, whose current is sinusoidally dependent on phase

$$I_{JJ} = I_c \sin \phi \tag{A.4}$$

where I_c is the junction critical current. Hence, by conservation of current and (A.3, A.4)

$$I'(\phi) = I_{JJ} - I_l = I_c \sin \phi + \frac{I_c}{\beta_L} \phi - \frac{1}{L_g} \Phi_e \tag{A.5}$$

where we defined the screening SQUID parameter

$$\beta_L \equiv 2\pi \frac{L_g I_c}{\Phi_0} = \frac{2e}{\hbar} L_g I_c < 1. \tag{A.6}$$

In the absence of current [14] $I = 0$, from (A.5) and using the relation of the phase- flux (A.1), we get the equation [11]

$$\phi + \beta_L \sin \phi = 2\pi \frac{\Phi_e}{\Phi_0} \tag{A.7}$$

Now from the circuit in Fig. A.1 (a), we focus only on the variation of the JJ phase associated φ with the (ac) current injected in the SQUID, so the current phase relation for the flux-biased SQUID becomes

$$I_S(\varphi) = I'(\phi + \varphi) - I'(\varphi) = I_c \left(\sin(\phi + \varphi) - \sin \phi \right) + \frac{I_c}{\beta_L} \varphi \tag{A.8}$$

where the inductance now is modified, taking into account not only the geometric one but adding the JJ inductance from (A.4)

$$\frac{1}{L} = \frac{1}{L_g} + \frac{1}{L_J} = \frac{1}{L_g} + \frac{2\pi}{\Phi_0} \frac{dI_{JJ}}{d\phi} = \frac{1}{L_g} (1 + \beta_L \cos \phi) \tag{A.9}$$

By expanding the asymmetric sinusoidal terms in (A.8) by Taylor series for small phase difference $\varphi \ll 1$, we get

$$\frac{I_S}{I_c} = \left(\frac{1}{\beta_L} + \cos \phi \right) \varphi - \frac{\beta}{\beta_L} \varphi^2 - \frac{\gamma}{\beta_L} \varphi^3 + O(\varphi^4), \tag{A.10}$$

where

$$\frac{\beta}{\beta_L} = \frac{1}{2} \sin \phi \qquad \frac{\gamma}{\beta_L} = \frac{1}{6} \cos \phi. \tag{A.11}$$

Obviously, for maximizing the quadratic non-linearity and reducing the cubic one, we use $\phi = \pi/2$ [15], which implies a magnetic flux of

$$\frac{\Phi_e}{\Phi_0} = \frac{\beta_L}{2\pi} + \frac{1}{4}. \tag{A.12}$$

where using (A.9) we observe that the total inductance is equal to the geometric one since $L_J = 0$. In order to create the poling necessary for the quasi-phase-matching, we simply need

to invert the configuration of the circuit as shown in Fig.A.1 (b,c). In this case still the current will be anticlockwise but the equation (A.7) will flip its signs, like

$$-\phi - \beta_L \sin\phi = 2\pi\frac{\Phi_e}{\Phi_0} \tag{A.13}$$

or equivalently, the external magnetic field will go opposite direction, or flipping $\Phi_e \to -\Phi_e$, from here, the phase $\phi \to -\phi$ and the quadratic coefficient will also flip its sign $\beta \to -\beta$.

A.2   Non-linear wave equation

We proceed to analyse an array of RF-SQUIDs or SNAILs, as shown in Fig. A.3, by using the Kirchhoff laws for current and voltage assuming the capacitance C_0 are the same for all cells.
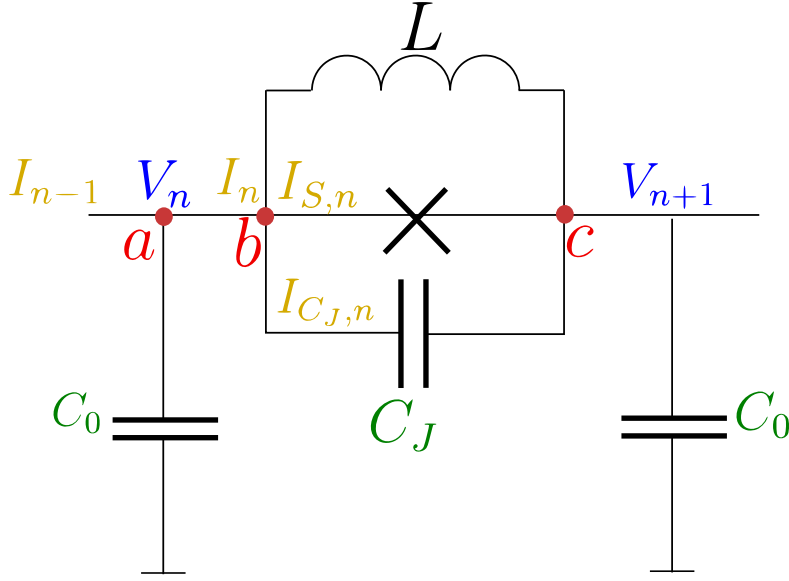
Figure A.2: One cell of the transmission line. Each cell has an RF-SQUID described in the previous figure, where the voltages and the currents are denoted by V and I, respectively.

The conservation of current on node a implies

$$I_n - I_{n-1} = -C_0\frac{dV_n}{dt} - \frac{V_n}{R} \tag{A.14}$$

In addition, from node b the conservation of the current is

$$I_n = I_{C_J,n} + I_{S,n}, \tag{A.15}$$

while the current of the capacitor $C_{J,n}$ is related to the potential difference

$$I_{(C_J),n} = -C_J\frac{d}{dt}(V_{n+1} - V_n). \tag{A.16}$$

Now we can combine the previous equations (A.14,A.15, A.16) we arrive to

$$-C_J\frac{d}{dt}(V_{n+1} - 2V_n + V_{n-1}) + I_{S,n} - I_{S,n-1} = -C_0\frac{dV_n}{dt} - \frac{V_n}{R} \tag{A.17}$$

Now we can use Faraday's law to relate the electromotive force (V_n) with the flux and the phase difference in each node

$$V_n \equiv \frac{d\Phi_e}{dt} = \frac{\Phi_0}{2\pi}\frac{d\varphi}{dt} \tag{A.18}$$

and the equation (A.10) upon into (A.17) to get the weakly nonlinear system of equations for the phase

$$-C_J \frac{d^2}{dt^2} (\varphi_{n+1} - 2\varphi_n + \varphi_{n-1}) + \frac{1}{L}(\varphi_{n+1} - 2\varphi_n + \varphi_{n-1}) - \beta \frac{1}{L}\left[(\varphi_{n+1} - \varphi_n)^2 - (\varphi_n - \varphi_{n-1})^2\right]$$

$$-\gamma \frac{1}{L}\left[(\varphi_{n+1} - \varphi_n)^3 - (\varphi_n - \varphi_{n-1})^3\right] = -C_0 \frac{d^2\varphi_n}{dt^2} - \frac{1}{R}\frac{d\varphi_n}{dt} \tag{A.19}$$

now following the continuous approximation described by [17], we can replace the discrete n by a continuous position $x \approx a/L$ where a is the length of each cell and L the full length of the transmission line, therefore we can approximate the finite difference terms as partial derivatives

$$\varphi_{n+1} - 2\varphi_n + \varphi_{n-1} \approx a^2 \frac{\partial\varphi}{\partial x^2} \tag{A.20}$$

$$(\varphi_{n+1} - \varphi_n)^2 - (\varphi_n - \varphi_{n-1})^2 \approx a^{n+1} \frac{\partial}{\partial x}\left[\left(\frac{\partial\varphi}{\partial x}\right)^n\right] \tag{A.21}$$

where substituting this approximations on (A.19) we obtain the non-linear wave equation

$$\frac{\partial^2\varphi}{\partial x^2} - \frac{1}{\omega_0^2}\frac{\partial^2\varphi}{\partial t^2} + \frac{1}{\omega_J^2}\frac{\partial^4\varphi}{\partial x^2 \partial t^2} + \tau_R \frac{\partial\varphi}{\partial t} - \beta\frac{\partial}{\partial x}\left[\left(\frac{\partial\varphi}{\partial x}\right)^2\right] - \gamma\frac{\partial}{\partial x}\left[\left(\frac{\partial\varphi}{\partial x}\right)^3\right] = 0 \tag{A.22}$$

where here we defined the cutoff frequency $\omega_0^{-2} \equiv LC_0$, the SQUID plasma frequency $\omega_J^{-2} \equiv LC_J$ and the time constant $\tau_R = L/R$. This equation can be reduced assuming first that dissipation by resistance is negligible $\tau_R \approx 0$ and using the condition (A.12) for making $\gamma \approx 0$ we get the equation

$$\frac{\partial^2\varphi}{\partial x^2} - \frac{1}{\omega_0^2}\frac{\partial^2\varphi}{\partial t^2} + \frac{1}{\omega_J^2}\frac{\partial^4\varphi}{\partial x^2 \partial t^2} = \beta(x)\frac{\partial}{\partial x}\left[\left(\frac{\partial\varphi}{\partial x}\right)^2\right] \tag{A.23}$$

By assuming [10] that the nonlinear component of (A.23) acts as a perturbation to homogeneous the superlinear equation

$$\frac{\partial^2\varphi}{\partial x^2} - \frac{1}{\omega_0^2}\frac{\partial^2\varphi}{\partial t^2} + \frac{1}{\omega_J^2}\frac{\partial^4\varphi}{\partial x^2 \partial t^2} = 0 \tag{A.24}$$

we can get the resulting dispersion equation

$$k(\omega) = \frac{\omega/\omega_0}{\sqrt{1 - \omega^2/\omega_J^2}} \tag{A.25}$$

that was obtained by using the plane wave $\varphi(x,t) = Ae^{i(kx-\omega t)}$. For frequencies much lower than the plasma frequency $\omega^2/\omega_J^2 \ll 1$, then eq (A.25) reduces to $k(\omega) \approx \omega/\omega_0$.

A.3   Coupled mode equations CME for SHG

We can find a system of coupled mode equations (CME) from the wave equation (A.23) by assuming an ansatz of a superposition of three waves: the pump, the idler and the signal, to achieve the second harmonic generation (SHG)

$$\varphi(x,t) = \sum_{m=\{i,s,p\}}\left[A_m(x)e^{i(k_m x - \omega_m t)} + \underbrace{A_m^*(x)e^{-i(k_m x - \omega_m t)}}_{\text{c.c.}}\right] \tag{A.26}$$

where k_m and A_m denotes the wave vectors and the amplitudes for the pump p, the signal s and the i idler, respectively. We assume that their respective frequencies ω_p, ω_s and ω_i are below the plasma frequency ω_J and much less than ω_0. We can substitute (A.26) on the superlinear part of the LHS of eq. (A.23) to get

$$\frac{\partial^2 \varphi}{\partial x^2} - \frac{1}{\omega_0^2}\frac{\partial^2 \varphi}{\partial t^2} + \frac{1}{\omega_J^2}\frac{\partial^4 \varphi}{\partial x^2 \partial t^2} = \sum_m \left[\left(1 - \frac{\omega_m^2}{\omega_J^2}\right)\left(\frac{d^2}{dx^2} + 2ik_m\frac{d}{dx} - k_m^2\right) + \frac{\omega_m^2}{\omega_0^2}\right] A_m e^{i\psi_m}$$

$$\approx \sum_m \left[\frac{1}{k_m^2}\frac{\omega_m^2}{\omega_0^2}\left(\frac{d^2}{dx^2} + 2ik_m\frac{d}{dx}\right)\right] A_m e^{i\psi_m} \qquad (A.27)$$

where we defined $\psi_m(x,t) \equiv k_m x - \omega_m t$, and used the dispersion equation (A.25) in the last equality. The slow varying amplitude limits the size of the derivatives of the amplitudes such that

$$\left|\frac{\partial^2 A_m}{\partial x^2}\right| \ll k_m \left|\frac{\partial A_m}{\partial x}\right| \ll k_m^2 |A_m| \qquad (A.28)$$

which applies to eq. (A.33) and using $k_m \approx \omega_m/\omega_0$ we get

$$\frac{\partial^2 \varphi}{\partial x^2} - \frac{1}{\omega_0^2}\frac{\partial^2 \varphi}{\partial t^2} + \frac{1}{\omega_J^2}\frac{\partial^4 \varphi}{\partial x^2 \partial t^2} \approx \sum_m 2ik_m \frac{dA_m}{dx} e^{i\psi_m} \qquad (A.29)$$

Explicitly the square of the derivative of the ansatz using the slow varying approximation (A.28)

$$\left(\frac{\partial \varphi}{\partial x}\right)^2 \approx \left(k_i(A_i e^{i\psi_i} - A_i^* e^{-i\psi_i}) + k_s(A_s e^{i\psi_s} - A_s^* e^{-i\psi_s}) + k_p(A_p e^{i\psi_p} - A_s^* e^{-i\psi_p})\right)^2$$

$$= A_i^2 k_i^2 e^{2i\psi_i} + A_s^2 k_s^2 e^{2i\psi_s} + A_p^2 k_p^2 e^{2i\psi_p} - |A_i|^2 k_i^2 - |A_s|^2 k_s^2 - |A_p|^2 k_p^2 + 2A_i A_p k_i k_p e^{i(\psi_i + \psi_p)}$$

$$- 2A_p A_i^* k_p k_i e^{i(-\psi_i + \psi_p)} + 2A_p A_s k_p k_s e^{i(\psi_p + \psi_s)} - 2A_s A_p^* k_s k_p e^{i(\psi_s - \psi_p)}$$

$$+ 2A_i A_s k_i k_s e^{i(\psi_i + \psi_s)} - 2A_i A_s^* k_i k_s e^{i(\psi_i - \psi_s)} + c.c. \qquad (A.30)$$

we are gonna focus our attention on the three-wave mixing where the following phase mismatch

$$\Delta \psi \equiv \psi_s + \psi_i - \psi_p \qquad (A.31)$$

is approximately small and constant. So by the rotating wave approximation, we can get rid of the non-resonant terms in the equation (A.30)

$$\left(\frac{\partial \varphi}{\partial x}\right)^2 \approx -2A_p A_i^* k_i k_p e^{i(-\psi_i + \psi_p)} - 2A_s A_p^* k_s k_p e^{i(\psi_s - \psi_p)} + 2A_i A_s k_i k_s e^{i(\psi_i + \psi_s)} + c.c \qquad (A.32)$$

Now we can derive it to get the right-hand side of (A.23) and also multiply our factor β

$$\beta\frac{\partial}{\partial x}\left[\left(\frac{\partial \varphi}{\partial x}\right)^2\right] \approx -2\beta i(-k_i + k_p)A_p A_i^* k_i k_p e^{i(-\psi_i + \psi_p)} - 2\beta i(k_s - k_p)A_s A_p^* k_s k_p e^{i(\psi_s - \psi_p)}$$

$$+ 2\beta i(k_i + k_s)A_i A_s k_i k_s e^{i(\psi_i + \psi_s)} + c.c \qquad (A.33)$$

From here, we can obtain the coupled mode equations; for instance let's derive one of them, from comparing the ψ_s phase on LHS (A.33) and making it equal to this last RHS (A.33) we get

$$2ik_s\frac{dA_s}{dx}e^{i\psi_s} = -2\beta i(-k_i + k_p)A_p A_I^* k_i k_p e^{i(-\psi_i + \psi_p)}$$

$$\implies \frac{dA_s}{dx} = -\beta A_p A_i^* k_i k_p e^{i(k_p - k_i - k_s)x} \qquad (A.34)$$

where we used that the phase mismatch $\Delta k = k_p - k_i - k_s$ is small in the coefficients. Finally, we can do the same process for the other phases to get the CMEs to describe the 3W parametric amplification [11, 10]

$$\frac{dA_s}{dx} = -\beta A_p A_i^* k_i k_p e^{i(k_p - k_i - k_s)x} \tag{A.35}$$

$$\frac{dA_i}{dx} = -\beta A_p A_s^* k_p k_s e^{i(k_p - k_s - k_i)x} \tag{A.36}$$

$$\frac{dA_p}{dx} = \beta A_i A_s k_i k_s e^{i(k_s + k_i - k_p)x}. \tag{A.37}$$

Zorin [15] and Yakoobi [17] redefine the coefficients in a half factor compared to our ansatz (A.26)

$$\varphi(x,t) = \sum_{m=\{i,s,p\}} \frac{1}{2} \left[A_m(x) e^{i(k_m x - \omega_m t)} + \underbrace{A_m^*(x) e^{-i(k_m x - \omega_m t)}}_{\text{c.c.}} \right] \tag{A.38}$$

this will modify the previous equations to a half-factor

$$\frac{dA_s}{dx} = -\frac{\beta}{2} A_p A_i^* k_i k_p e^{i\Delta kx}$$

$$\frac{dA_i}{dx} = -\frac{\beta}{2} A_p A_s^* k_p k_s e^{i\Delta kx}$$

$$\frac{dA_p}{dx} = \frac{\beta}{2} A_i A_s k_i k_s e^{-i\Delta kx}. \tag{A.39}$$

where we used the difference in the wave vector as

$$\Delta k \equiv k_p - k_i - k_s. \tag{A.40}$$

We need to be careful here; the previous analysis was done assuming β the quadratic Kerr nonlinear coefficient is constant. However, in our periodic poling, we will use a square wave for our $\beta(x) \sim \text{sgn}(\sin \alpha x)$. The expressions overall won't change since we are going to assume that the transitions in the square wave are so sharp that its derivative remains approximately zero.

A.4 Analytic solution for constant β nonlinearity

Using a similar method given by [20, 21], we can solve analytically the coupled differential equations (A.39) first by assuming the signal intensity (squared norm of the amplitude) is much greater than the pump and the idler

$$|A_s|^2 = |A_{s0}|^2 \sim \text{constant}, \qquad |A_s|^2 \gg |A_i|^2, \qquad |A_s|^2 \gg |A_p|^2 \tag{A.41}$$

such that the system (A.39) is reduced to

$$\frac{dA_i}{dx} = -\frac{\beta}{2} A_{s0}^* k_p k_s A_p e^{i\Delta kx} \tag{A.42}$$

$$\frac{dA_p}{dx} = \frac{\beta}{2} A_{s0} k_i k_s A_i e^{-i\Delta kx}. \tag{A.43}$$

We start deriving the equation for dA_i/dx (A.39) and substituting (A.42)

$$\frac{d^2 A_i}{dx^2} = -\frac{\beta}{2} A_{s0}^* k_p k_s \left(\frac{dA_p}{dx} e^{i\Delta kx} + i\Delta k A_p e^{i\Delta kx} \right) = -\frac{\beta}{2} A_{s0}^* k_p k_s \frac{dA_p}{dx} e^{i\Delta kx} + i\Delta k \frac{dA_i}{dx}$$

$$= -\left(\frac{\beta}{2} \right)^2 |A_{s0}|^2 k_s k_i k_p A_i + i\Delta k \frac{dA_i}{dx} = -\kappa^2 A_i + i\Delta k \frac{dA_i}{dx} \tag{A.44}$$
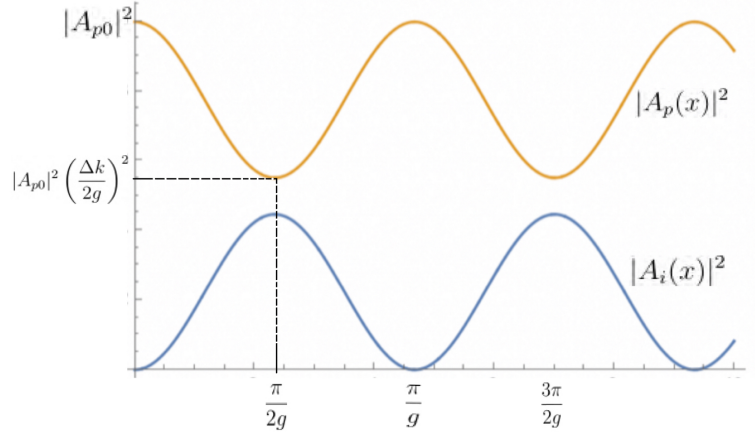
Figure A.3: Pump $|A_p(x)|^2$ and idler $|A_i(x)|^2$ intensity (square of the amplitude) as a function of the position x. We can note from her that the decoherence length $\pi/2g$.

where we defined

$$\kappa^2 \equiv \left(\frac{\beta}{2}\right)^2 |A_{s0}|^2 k_s^2 k_i k_p \tag{A.45}$$

Now we can propose an ansatz of the form $A_i \sim e^{i\lambda x}$, so the factor λ in the previous equation satisfies the polynomial

$$(i\lambda)^2 = -\kappa^2 + (i\lambda)(i\Delta k) \implies \lambda^2 - \Delta k\lambda - \kappa^2 = 0 \implies \lambda = \frac{\Delta k}{2} \pm g \text{ where } g = \sqrt{\left(\frac{\Delta k}{2}\right)^2 + \kappa^2}. \tag{A.46}$$

Thus taking the initial condition $A_i(0) = 0$, we arrive to the solution for the pump amplitude

$$A_i(x) = A \sin(gx) e^{i\frac{\Delta k}{2}x} \implies |A_i(x)|^2 = |A|^2 \sin^2(gx), \tag{A.47}$$

where A will be determined by the pump amplitude obtained by (A.42)

$$A_p(x) = -\frac{2}{\beta} \frac{1}{A_{s0}^* k_p k_s} \frac{dA_i}{dx} e^{-i\Delta kx} = -\frac{2}{\beta} \frac{Ag}{A_{s0}^* k_p k_s} \left(\cos gx + i\frac{\Delta k}{2g} \sin gx\right) e^{i\frac{\Delta k}{2}x} \tag{A.48}$$

with the initial given condition $A_p(0) = A_{p0}$ we arrive to a pump intensity

$$|A_p(x)|^2 = |A_{p0}|^2 \left(\cos^2 gx + \left(\frac{\Delta k}{2g}\right)^2 \sin^2 gx\right) \tag{A.49}$$

and (A.47) can be rewritten in terms of the initial pump, such that

$$|A_i(x)|^2 = \left(\frac{\beta}{2g}\right)^2 |A_{p0}|^2 |A_{s0}|^2 k_p^2 k_s^2 \sin^2(gx). \tag{A.50}$$

A.5 Quasi-phase matching for SHG and weak idler amplitude.

Up until now, we have assumed β constant; in this chapter, we are going to analyze the quasi-phase matching by assuming that the idler signal or the second harmonic field is small in comparison with the pump and signal intensity which remain similar in magnitude and constant, i.e.

$$|A_s|^2 = |A_{s0}|^2 \approx |A_p|^2 = |A_{p0}|^2 \sim \text{constant}, \qquad |A_s|^2 = |A_p|^2 \gg |A_i|^2, \tag{A.51}$$

29

such that the system gets reduced to only one equation (A.42) that is

$$\frac{dA_p}{dx} \approx \frac{dA_s}{dx} \approx 0 \qquad \frac{dA_i}{dx} = -\frac{\beta}{2}|A_{p0}|^2 k_p k_s e^{i\Delta kx} = -\Gamma\beta e^{i\Delta kx} \tag{A.52}$$

where we define the factor, described by [22],

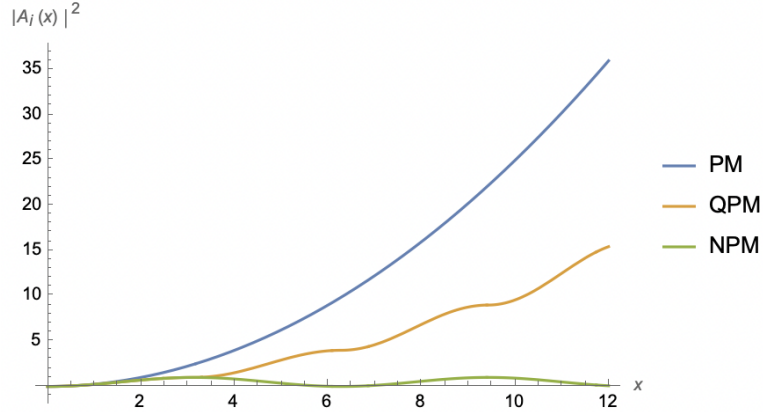$$\Gamma = \frac{|A_{p0}|^2}{2} k_p k_s. \tag{A.53}$$

Figure A.4: Quasi-phase matching QPM: effect on the phase matching PM growth of second harmonic intensity $A_i(x)$ (A.56) as a function of the position due to a periodic poling at coherence length l_c (A.58). It is also superimposed the result when $\beta = 1$, then no phase matching NPM growth will occur.

Now if we **assume** $\beta = 1$, we can integrate the equation (A.52) to get

$$A_i(x) = -\frac{\Gamma}{i\Delta k}(e^{i\Delta k} - 1) = -\frac{2\Gamma}{\Delta k} e^{i(\Delta k/2)x} \sin(\Delta k/2)x \tag{A.54}$$

whose intensity (square amplitude) is

$$|A_i(x)|^2 = \left(\frac{2\Gamma}{\Delta k}\right)^2 \sin^2(\Delta k/2)x = \Gamma^2 x^2 \mathrm{sinc}^2\left(\frac{\Delta k}{2}x\right) \tag{A.55}$$

where the sinc function $\mathrm{sinc}(x) = \sin x/x$ tends to one in the limit of $\Delta k \to 0$, where we can see that the second harmonic intensity increases quadratically with the length, this feature is known as **phase-matching**:

$$\lim_{\Delta k \to 0} |A_i(L)|^2 = \Gamma^2 L^2. \tag{A.56}$$

From the non-phase matching $\Delta k \neq 0$ idler intensity (A.55), we can get the coherence length l_c, that is, the length from zero to the maximum amplitude, i.e.

$$\frac{\Delta k}{2}l_c = \frac{\pi}{2} \implies l_c = \frac{\pi}{\Delta k}, \tag{A.57}$$

and from this distance, we can define the domains for the periodic poling, such that

$$\beta(x) = \mathrm{sgn}\left[\sin(\pi/l_c)x\right] \tag{A.58}$$

which is a square function, with domains of length l_c. Check that approximately this discontinuous function has a zero derivative almost everywhere except in a zero-measure discontinuous

domain $\{x = nl_c : n \in \mathbb{Z}\}$. Therefore the set of coupled differential equations (A.39) are still valid.

Integrating (A.52) by assuming periodic poling (A.58) we get

$$A_i(L) = -\Gamma \int_0^L \beta(z)e^{i\Delta kz}dz = -\Gamma \sum_{n=0}^N \int_{nl_c}^{(n+1)l_c} (-1)^n e^{i\Delta kz}dz - \Gamma \sum_{n=0}^N (-1)^n \frac{e^{i\Delta kl_c n}}{i\Delta k}(e^{i\Delta kl_c} - 1)$$

$$= \frac{2\Gamma}{i\Delta k}\sum_{n=0}^N (-1)^{2n} = \frac{2}{i\Delta k}(N+1) = \frac{2\Gamma}{i\pi}(N+1)l_c \implies |A_i(L)|^2 = \left(\frac{2}{\pi}\Gamma L\right)^2 \tag{A.59}$$

where we used $L = (N+1)l_c$ and (A.57), getting a gain $4/\pi^2 \approx 41\%$, compared to a conventionally phase matched interaction (A.56).

A.5.1 Quasiphase mathching in pump depletion

Moreover, in this section, we discuss the coherence length for the general CME setting (A.42) and (A.43). In complete quasi-phase-matching, we want to keep increasing the idler amplitude until pump depletion. From the analytical solution for the amplitude (A.50) we can note that the amplitude is proportional to $\sin^2(gx)$, giving us therefore a coherence length

$$l_c = \frac{\pi}{2g}, \tag{A.60}$$

to be substituted on the periodic poling function (A.58).

Appendix B

CME 5

Here we write the Coupled mode equations for five tones derived by [7]. They are derived from solving the non-linear wave equation (A.23) but now proposing a different ansatz (A.26) that includes extra terms

$$\varphi(x,t) = \sum_{\substack{m=i,s,p,p+i,p+s,2p+i,2p+s,3p, \\ 3p+i,3p+s,4p,4p+i,4p+s,5p}} \left[A_m(x)e^{i(k_m x - \omega_m t)} + \underbrace{A_m^*(x)e^{-i(k_m x - \omega_m t)}}_{\text{c.c.}} \right] \tag{B.1}$$

and again, we assume the slow varying approximation (A.28) such that we get a first-order system of fifteen coupled differential equations

$$\frac{dA_i}{dx} = \frac{\beta}{2} \left(k_s k_p A_p A_s^* e^{i(k_p - k_s)x} + k_{p+i} k_p A_{p+i} A_p^* e^{i(k_{p+i} - k_p)x} \right.$$
$$+ k_{2p} k_{p+s} A_{2p} A_{p+s}^* e^{i(k_{2p} - k_{p+s})x} + k_{2p+i} k_{2p} A_{2p+i} A_{2p}^* e^{i(k_{2p+i} - k_{2p})x}$$
$$+ k_{3p} k_{2p+s} A_{3p} A_{2p+s}^* e^{i(k_{3p} - k_{2p+s})x} + k_{3p+i} k_{3p} A_{3p+i} A_{3p}^* e^{i(k_{3p+i} - k_{3p})x}$$
$$+ k_{4p} k_{3p+s} A_{4p} A_{3p+s}^* e^{i(k_{4p} - k_{3p+s})x} + k_{4p+i} k_{4p} A_{4p+i} A_{4p}^* e^{i(k_{4p+i} - k_{4p})x}$$
$$\left. + k_{5p} k_{4p+s} A_{5p} A_{4p+s}^* e^{i(k_{5p} - k_{4p+s})x} \right) e^{-ik_i x}, \tag{B.2}$$

$$\frac{dA_s}{dx} = \frac{\beta}{2} \left(k_i k_p A_p A_i^* e^{i(k_p - k_i)x} + k_{p+s} k_p A_{p+s} A_p^* e^{i(k_{p+s} - k_p)x} \right.$$
$$+ k_{2p} k_{p+i} A_{2p} A_{p+i}^* e^{i(k_{2p} - k_{p+i})x} + k_{2p+s} k_{2p} A_{2p+s} A_{2p}^* e^{i(k_{2p+s} - k_{2p})x}$$
$$+ k_{3p} k_{2p+i} A_{3p} A_{2p+i}^* e^{i(k_{3p} - k_{2p+i})x} + k_{3p+s} k_{3p} A_{3p+s} A_{3p}^* e^{i(k_{3p+s} - k_{3p})x}$$
$$+ k_{4p} k_{3p+i} A_{4p} A_{3p+i}^* e^{i(k_{4p} - k_{3p+i})x} + k_{4p+s} k_{4p} A_{4p+s} A_{4p}^* e^{i(k_{4p+s} - k_{4p})x}$$
$$\left. + k_{5p} k_{4p+i} A_{5p} A_{4p+i}^* e^{i(k_{5p} - k_{4p+i})x} \right) e^{-ik_s x}, \tag{B.3}$$

$$\frac{dA_p}{dx} = \frac{\beta}{2} \left(-k_i k_s A_i A_s e^{i(k_i + k_s)x} + k_{p+i} k_i A_{p+i} A_i^* e^{i(k_{p+i} - k_i)x} \right.$$
$$+ k_{p+s} k_s A_{p+s} A_s^* e^{i(k_{p+s} - k_s)x} + k_{2p} k_p A_{2p} A_p^* e^{i(k_{2p} - k_p)x}$$
$$+ k_{2p+i} k_{p+i} A_{2p+i} A_{p+i}^* e^{i(k_{2p+i} - k_{p+i})x} + k_{2p+s} k_{p+s} A_{2p+s} A_{p+s}^* e^{i(k_{2p+s} - k_{p+s})x}$$
$$+ k_{3p} k_{2p} A_{3p} A_{2p}^* e^{i(k_{3p} - k_{2p})x} + k_{3p+i} k_{2p+i} A_{3p+i} A_{2p+i}^* e^{i(k_{3p+i} - k_{2p+i})x}$$
$$+ k_{3p+s} k_{2p+s} A_{3p+s} A_{2p+s}^* e^{i(k_{3p+s} - k_{2p+s})x} + k_{4p} k_{3p} A_{4p} A_{3p}^* e^{i(k_{4p} - k_{3p})x}$$
$$+ k_{4p+i} k_{3p+i} A_{4p+i} A_{3p+i}^* e^{i(k_{4p+i} - k_{3p+i})x} + k_{4p+s} k_{3p+s} A_{4p+s} A_{3p+s}^* e^{i(k_{4p+s} - k_{3p+s})x}$$
$$\left. + k_{5p} k_{4p} A_{5p} A_{4p}^* e^{i(k_{5p} - k_{4p})x} \right) e^{-ik_p x} \tag{B.4}$$

$$\frac{dA_{p+i}}{dx} = \frac{\beta}{2} \left(-k_i k_p A_i A_p e^{i(k_i + k_p)x} + k_{2p} k_s A_{2p} A_s^* e^{i(k_{2p} - k_s)x} \right.$$
$$+ k_{2p+i} k_p A_{2p+i} A_p^* e^{i(k_{2p+i} - k_p)x} + k_{3p} k_{p+s} A_{3p} A_{p+s}^* e^{i(k_{3p} - k_{p+s})x}$$
$$+ k_{3p+i} k_{2p} A_{3p+i} A_{2p}^* e^{i(k_{3p+i} - k_{2p})x} + k_{4p} k_{2p+s} A_{4p} A_{2p+s}^* e^{i(k_{4p} - k_{2p+s})x}$$
$$\left. + k_{4p+i} k_{3p} A_{4p+i} A_{3p}^* e^{i(k_{4p+i} - k_{3p})x} + k_{5p} k_{3p+s} A_{5p} A_{3p+s}^* e^{i(k_{5p} - k_{3p+s})x} \right) e^{-ik_{p+i} x}, \tag{B.5}$$

$$\frac{dA_{p+s}}{dx} = \frac{\beta}{2} \left(-k_s k_p A_s A_p e^{i(k_s + k_p)x} + k_{2p} k_i A_{2p} A_i^* e^{i(k_{2p} - k_i)x} \right.$$
$$+ k_{2p+s} k_p A_{2p+s} A_p^* e^{i(k_{2p+s} - k_p)x} + k_{3p} k_{p+i} A_{3p} A_{p+i}^* e^{i(k_{3p} - k_{p+i})x}$$
$$+ k_{3p+s} k_{2p} A_{3p+s} A_{2p}^* e^{i(k_{3p+s} - k_{2p})x} + k_{4p} k_{2p+i} A_{4p} A_{2p+i}^* e^{i(k_{4p} - k_{2p+i})x}$$
$$\left. + k_{4p+s} k_{3p} A_{4p+s} A_{3p}^* e^{i(k_{4p+s} - k_{3p})x} + k_{5p} k_{3p+i} A_{5p} A_{3p+i}^* e^{i(k_{5p} - k_{3p+i})x} \right) e^{-ik_{p+s} x}, \tag{B.6}$$

$$\frac{dA_{2p}}{dx} = \frac{\beta}{2}\left(-k_i k_{p+s} A_i A_{p+s} e^{i(k_i+k_{p+s})x} - k_s k_{p+i} A_s A_{p+i} e^{i(k_s+k_{p+i})x}\right.$$
$$-\frac{k_p^2}{A_p^2} 2 e^{i(k_p+k_p)x} + k_{2p+i} k_i A_{2p+i} A_i^* e^{i(k_{2p+i}-k_i)x}$$
$$+ k_{2p+2} k_s A_{2p+s} A_s^* e^{i(k_{2p+s}-k_s)x} + k_{3p} k_p A_{3p} A_p^* e^{i(k_{3p}-k_p)x}$$
$$+ k_{3p+i} k_{p+i} A_{3p+i} A_{p+i}^* e^{i(k_{3p+i}-k_{p+i})x} + k_{3p+s} k_{p+s} A_{3p+s} A_{p+s}^* e^{i(k_{3p+s}-k_{p+s})x}$$
$$+ k_{4p} k_{2p} A_{4p} A_{2p}^* e^{i(k_{4p}-k_{2p})x} + k_{4p+i} k_{2p+i} A_{4p+i} A_{2p+i}^* e^{i(k_{4p+i}-k_{2p+i})x}$$
$$\left.+ k_{4p+s} k_{2p+s} A_{4p+s} A_{2p+s}^* e^{i(k_{4p+s}-k_{2p+s})x} + k_{5p} k_{3p} A_{5p} A_{3p}^* e^{i(k_{5p}-k_{3p})x}\right) e^{-ik_{2p}x} \tag{B.7}$$

$$\frac{dA_{2p+i}}{dx} = \frac{\beta}{2}\left(-k_i k_{2p} A_i A_{2p} e^{i\left(k_i+k_{2p}\right)x} - k_p k_{p+i} A_p A_{p+i} e^{i\left(k_p+k_{p+i}\right)x}\right.$$
$$+ k_{3p} k_s A_{3p} A_s^* e^{i\left(k_{3p}-k_s\right)x} + k_{3p+i} k_p A_{3p+i} A_p^* e^{i\left(k_{3p+i}-k_p\right)x}$$
$$+ k_{4p} k_{p+s} A_{4p} A_{p+s}^* e^{i\left(k_{4p}-k_{p+s}\right)x} + k_{4p+i} k_{2p} A_{4p+i} A_{2p}^* e^{i\left(k_{4p+i}-k_{2p}\right)x}$$
$$\left.+ k_{5p} k_{2p+s} A_{5p} A_{2p+s}^* e^{i\left(k_{5p}-k_{2p+s}\right)x}\right) e^{-ik_{2p+i}x}, \tag{B.8}$$

$$\frac{dA_{2p+s}}{dx} = \frac{\beta}{2}\left(-k_s k_{2p} A_s A_{2p} e^{i\left(k_s+k_{2p}\right)x} - k_p k_{p+s} A_p A_{p+s} e^{i\left(k_p+k_{p+s}\right)x}\right.$$
$$+ k_{3p} k_i A_{3p} A_i^* e^{i\left(k_{3p}-k_i\right)x} + k_{3p+s} k_p A_{3p+s} A_p^* e^{i\left(k_{3p+s}-k_p\right)x}$$
$$+ k_{4p} k_{p+i} A_{4p} A_{p+i}^* e^{i\left(k_{4p}-k_{p+i}\right)x} + k_{4p+s} k_{2p} A_{4p+s} A_{2p}^* e^{i\left(k_{4p+s}-k_{2p}\right)x}$$
$$\left.+ k_{5p} k_{2p+i} A_{5p} A_{2p+i}^* e^{i\left(k_{5p}-k_{2p+i}\right)x}\right) e^{-ik_{2p+s}x}, \tag{B.9}$$

$$\frac{dA_{3p}}{dx} = \frac{\beta}{2}\left(-k_i k_{2p+s} A_i A_{2p+s} e^{i\left(k_i+k_{2p+s}\right)x} - k_s k_{2p+i} A_s A_{2p+i} e^{i\left(k_s+k_{2p+i}\right)x}\right.$$
$$- k_p k_{2p} A_p A_{2p} e^{i\left(k_p+k_{2p}\right)x} - k_{p+i} k_{p+s} A_{p+i} A_{p+s} e^{i\left(k_{p+i}+k_{p+s}\right)x}$$
$$+ k_{3p+i} k_i A_{3p+i} A_i^* e^{i\left(k_{3p+i}-k_i\right)x} + k_{3p+s} k_s A_{3p+s} A_s^* e^{i\left(k_{3p+s}-k_s\right)x}$$
$$+ k_{4p} k_p A_{4p} A_p^* e^{i\left(k_{4p}-k_p\right)x} + k_{4p+i} k_{p+i} A_{4p+i} A_{p+i}^* e^{i\left(k_{4p+i}-k_{p+i}\right)x}$$
$$\left.+ k_{4p+s} k_{p+s} A_{4p+s} A_{p+s}^* e^{i\left(k_{4p+s}-k_{p+s}\right)x} + k_{5p} k_{2p} A_{5p} A_{2p}^* e^{i\left(k_{5p}-k_{2p}\right)x}\right) e^{-ik_{3p}x}, \tag{B.10}$$

$$\frac{dA_{3p+i}}{dx} = \frac{\beta}{2}\left(-k_i k_{3p} A_i A_{3p} e^{i\left(k_i+k_{3p}\right)x} - k_p k_{2p+i} A_p A_{2p+i} e^{i\left(k_p+k_{2p+i}\right)x}\right.$$
$$- k_{p+i} k_{2p} A_{p+i} A_{2p} e^{i\left(k_{p+i}+k_{2p}\right)x} + k_{4p} k_S A_{4p} A_S^* e^{i\left(k_{4p}-k_s\right)x}$$
$$\left.+ k_{4p+i} k_p A_{4p+i} A_p^* e^{i\left(k_{4p+i}-k_p\right)x} + k_{5p} k_{p+s} A_{5p} A_{p+s}^* e^{i\left(k_{5p}-k_{p+s}\right)x}\right) e^{-ik_{3p+i}x} \tag{B.11}$$

$$
\begin{aligned}
\frac{dA_{3p+s}}{dx} =& \frac{\beta}{2}\left(-k_s k_{3p} A_s A_{3p} e^{i\left(k_s+k_{3p}\right)x} - k_p k_{2p+s} A_p A_{2p+s} e^{i\left(k_p+k_{2p+s}\right)x}\right.\\
&- k_{p+s} k_{2p} A_{p+s} A_{2p} e^{i\left(k_{p+s}+k_{2p}\right)x} + k_{4p} k_i A_{4p} A_i^* e^{i\left(k_{4p}-k_i\right)x}\\
&\left.+ k_{4p+s} k_p A_{4p+s} A_p^* e^{i\left(k_{4p+s}-k_p\right)x} + k_{5p} k_{p+i} A_{5p} A_{p+i}^* e^{i\left(k_{5p}-k_{p+i}\right)x}\right) e^{-ik_{3p+s}x},
\end{aligned}
\tag{B.12}
$$

$$
\begin{aligned}
\frac{dA_{4p}}{dx} =& \frac{\beta}{2}\left(-k_i k_{3p+s} A_i A_{3p+s} e^{i\left(k_i+k_{3p+s}\right)x} - k_s k_{3p+i} A_s A_{3p+i} e^{i\left(k_s+k_{3p+i}\right)x}\right.\\
&- k_p k_{3p} A_p A_{3p} e^{i\left(k_p+k_{3p}\right)x} - k_{p+i} k_{2p+s} A_{p+i} A_{2p+s} e^{i\left(k_{p+i}+k_{2p+s}\right)x}\\
&- k_{p+s} k_{2p+i} A_{p+s} A_{2p+i} e^{i\left(k_{p+s}+k_{2p+i}\right)x} - \frac{k_{2p}^2 A_{2p}^2}{2} e^{i\left(k_{2p}+k_{2p}\right)x}\\
&+ k_{4p+i} k_i A_{4p+i} A_i^* e^{i\left(k_{4p+i}-k_i\right)x} + k_{4p+s} k_s A_{4p+s} A_s^* e^{i\left(k_{4p+s}-k_s\right)x}\\
&\left.+ k_{5p} k_p A_{5p} A_p^* e^{i\left(k_{5p}-k_p\right)x}\right) e^{-ik_{4p}x},
\end{aligned}
\tag{B.13}
$$

$$
\begin{aligned}
\frac{dA_{4p+i}}{dx} =& \frac{\beta}{2}\left(-k_i k_{4p} A_i A_{4p} e^{i\left(k_i+k_{4p}\right)x} - k_p k_{3p+i} A_p A_{3p+i} e^{i\left(k_p+k_{3p+i}\right)x}\right.\\
&- k_{p+i} k_{3p} A_{p+i} A_{3p} e^{i\left(k_{p+i}+k_{3p}\right)x} - k_{2p} k_{2p+i} A_{2p} A_{2p+i} e^{i\left(k_{2p}+k_{2p+i}\right)x}\\
&\left.+ k_{5p} k_s A_{5p} A_s^* e^{i\left(k_{5p}-k_s\right)x}\right) e^{-ik_{4p+i}x},
\end{aligned}
\tag{B.14}
$$

$$
\begin{aligned}
\frac{dA_{4p+s}}{dx} =& \frac{\beta}{2}\left(-k_s k_{4p} A_s A_{4p} e^{i\left(k_s+k_{4p}\right)x} - k_p k_{3p+s} A_p A_{3p+s} e^{i\left(k_p+k_{3p+s}\right)x}\right.\\
&- k_{p+s} k_{3p} A_{p+s} A_{3p} e^{i\left(k_{p+s}+k_{3p}\right)x} - k_{2p} k_{2p+s} A_{2p} A_{2p+s} e^{i\left(k_{2p}+k_{2p+s}\right)x}\\
&\left.+ k_{5p} k_i A_{5p} A_i^* e^{i\left(k_{5p}-k_i\right)x}\right) e^{-ik_{4p+s}x},
\end{aligned}
\tag{B.15}
$$

$$
\begin{aligned}
\frac{dA_{5p}}{dx} =& \frac{\beta}{2}\left(-k_i k_{4p+s} A_i A_{4p+s} e^{i\left(k_i+k_{4p+s}\right)x} - k_s k_{4p+i} A_s A_{4p+i} e^{i\left(k_s+k_{4p+i}\right)x}\right.\\
&- k_p k_{4p} A_p A_{4p} e^{i\left(k_p+k_{4p}\right)x} - k_{p+i} k_{3p+s} A_{p+i} A_{3p+s} e^{i\left(k_{p+i}+k_{3p+s}\right)x}\\
&- k_{p+s} k_{3p+i} A_{p+s} A_{3p+i} e^{i\left(k_{p+s}+k_{3p+i}\right)x} - k_{2p} k_{3p} A_{2p} A_{3p} e^{i\left(k_{2p}+k_{3p}\right)x}\\
&\left.- k_{2p+i} k_{2p+s} A_{2p+i} A_{2p+s} e^{i\left(k_{2p+i}+k_{2p+s}\right)x}\right) e^{-ik_{5p}x}.
\end{aligned}
\tag{B.16}
$$

Bibliography

[1] Baleegh Abdo et al. "Active protection of a superconducting qubit with an interferometric Josephson isolator". In: *Nature Communications* 10.1 (July 2019). ISSN: 2041-1723. DOI: 10.1038/s41467-019-11101-3. URL: http://dx.doi.org/10.1038/s41467-019-11101-3.

[2] F. Lecocq et al. "Nonreciprocal Microwave Signal Processing with a Field-Programmable Josephson Amplifier". In: *Physical Review Applied* 7.2 (Feb. 2017). ISSN: 2331-7019. DOI: 10.1103/physrevapplied.7.024028. URL: http://dx.doi.org/10.1103/PhysRevApplied.7.024028.

[3] Qiushi Guo et al. "Femtojoule femtosecond all-optical switching in lithium niobate nanophotonics". In: *Nature Photonics* 16.9 (2022), pp. 625–631.

[4] Joseph Kerckhoff et al. "On-Chip Superconducting Microwave Circulator from Synthetic Rotation". In: *Physical Review Applied* 4.3 (Sept. 2015). ISSN: 2331-7019. DOI: 10.1103/physrevapplied.4.034002. URL: http://dx.doi.org/10.1103/PhysRevApplied.4.034002.

[5] N. R. Bernier et al. "Nonreciprocal reconfigurable microwave optomechanical circuit". In: *Nature Communications* 8.1 (Sept. 2017). ISSN: 2041-1723. DOI: 10.1038/s41467-017-00447-1. URL: http://dx.doi.org/10.1038/s41467-017-00447-1.

[6] Leonardo Ranzani et al. "Wideband isolation by frequency conversion in a Josephson-junction transmission line". In: *Physical Review Applied* 8.5 (2017), p. 054035.

[7] Alexander B. Zorin. "Quasi-phasematching in a poled Josephson traveling-wave parametric amplifier with three-wave mixing". In: *Applied Physics Letters* 118.22 (2021).

[8] Katia Gallo et al. "All-optical diode in a periodically poled lithium niobate waveguide". In: *Applied Physics Letters* 79.3 (2001), pp. 314–316.

[9] Katia Gallo and Gaetano Assanto. "All-optical diode based on second-harmonic generation in an asymmetric waveguide". In: *JOSA B* 16.2 (1999), pp. 267–269.

[10] T. Dixon et al. "Capturing Complex Behavior in Josephson Traveling-Wave Parametric Amplifiers". In: *Phys. Rev. Appl.* 14 (3 Sept. 2020), p. 034058. DOI: 10.1103/PhysRevApplied.14.034058. URL: https://link.aps.org/doi/10.1103/PhysRevApplied.14.034058.

[11] A. B. Zorin. "Josephson Traveling-Wave Parametric Amplifier with Three-Wave Mixing". In: *Phys. Rev. Appl.* 6 (3 Sept. 2016), p. 034006. DOI: 10.1103/PhysRevApplied.6.034006. URL: https://link.aps.org/doi/10.1103/PhysRevApplied.6.034006.

[12] C. Macklin et al. "A near–quantum-limited Josephson traveling-wave parametric amplifier". In: *Science* 350.6258 (2015), pp. 307–310. DOI: 10.1126/science.aaa8525. eprint: https://www.science.org/doi/pdf/10.1126/science.aaa8525. URL: https://www.science.org/doi/abs/10.1126/science.aaa8525.

[13] J. Y. Mutus et al. "Strong environmental coupling in a Josephson parametric amplifier". In: *Applied Physics Letters* 104.26 (June 2014). ISSN: 1077-3118. DOI: 10.1063/1.4886408. URL: http://dx.doi.org/10.1063/1.4886408.

[14] John Clarke and Alex Braginski. *The SQUID Handbook*. Germany: Wiley-VCH, 2004.

[15] A.B. Zorin. "Flux-Driven Josephson Traveling-Wave Parametric Amplifier". In: *Phys. Rev. Appl.* 12 (4 Oct. 2019), p. 044051. DOI: 10.1103/PhysRevApplied.12.044051. URL: https://link.aps.org/doi/10.1103/PhysRevApplied.12.044051.

[16] Eli Levenson-Falk. "Static and Microwave Transport Properties of Aluminum Nanobridge Josephson Junctions". PhD thesis. UC Berkeley, 2013.

[17] O. Yaakobi et al. "Parametric amplification in Josephson junction embedded transmission lines". In: *Phys. Rev. B* 87 (14 Apr. 2013), p. 144301. DOI: 10.1103/PhysRevB.87.144301. URL: https://link.aps.org/doi/10.1103/PhysRevB.87.144301.

[18] Konstantin Likharev. *Dynamics of Josephson Junctions and Circuits*. Amsterdam: Gordon and Breach Science Publishers, 1986.

[19] L. Jackel, T. Clark, and R. Buhrman. "Current-phase relations and noise in rf biased squids". In: *IEEE Transactions on Magnetics* 11.2 (1975), pp. 732–735. DOI: 10.1109/TMAG.1975.1058695.

[20] Robert Boyd. *Nonlinear Optics*. 3rd ed. USA: Academic Press, 2008.

[21] Chia Wei Wade Hsu. *Lecture notes in Non-linear optics*. Aug. 2023.

[22] M.M. Fejer et al. "Quasi-phase-matched second harmonic generation: tuning and tolerances". In: *IEEE Journal of Quantum Electronics* 28.11 (1992), pp. 2631–2654. DOI: 10.1109/3.161322.